Characterization of Slat Noise Radiation from a High-Lift Common Research Model

William M. Humphreys, Jr.*, David P. Lockard‡, and Christopher J. Bahr§
NASA Langley Research Center, Hampton, Virginia 23681

A test campaign was conducted in the open-jet test section of the NASA Langley 14- by 22-Foot Subsonic Tunnel on a 10%-scale, semispan version of a High-Lift Common Research Model incorporating a leading-edge slat, trailing-edge flap and removable high-fidelity main landing gear. Computational simulations were used to support the model development, provide important information such as load distributions along the high-lift elements, and aid in the design of noise reduction devices. Aerodynamic and far field acoustic measurements were obtained on baseline and acoustically treated model configurations using an ensemble of time-averaged and unsteady surface pressure sensors paired with a traversing 97-microphone phased array viewing the pressure side of the airframe. A deconvolution method incorporating corrections for shear layer acoustic wave decorrelation was employed to determine the locations and strengths of relevant noise sources along the span of the slat and in the vicinity of the flap edges and landing gear. The main goal of the test campaign was to use the surface pressure and array data to evaluate the effectiveness of various slat noise reduction concepts. It was found that slat-gap fillers produced significant broadband noise reduction with minimal aerodynamic performance penalties for all Mach numbers and airfoil angles of attack that were investigated. The test campaign clearly demonstrated the noise reduction benefits that can be obtained by applying appropriate treatments to leading-edge slats on commercial transport-class aircraft.

This paper is the merger of two papers previously presented by the authors at the 28th AIAA/CEAS Aeroacoustics Conference in Southampton, UK in 2022: (1) AIAA Paper 2022-2805, and (2) AIAA Paper 2022-2806.

*Research Directorate; william.m.humphreys@nasa.gov. Associate Fellow AIAA (Corresponding Author).
‡Computational AeroSciences Branch. Associate Fellow AIAA.
§Aeroacoustics Branch. Associate Fellow AIAA.

Nomenclature

C_p	=	coefficient of pressure
f	=	frequency, Hertz
f_m	=	model scale frequency, Hertz
CSM	=	Cross Spectral Matrix
CRM-HL	=	High-Lift Common Research Model
DAMAS	=	Deconvolution Approach for the Mapping of Acoustic Sources
FSS	=	Full-Span Slat
M	=	Mach number
MCF	=	Mutual Coherence Function
MLG	=	Main Landing Gear
PSD	=	Power Spectral Density
PSS	=	Part-Span Slat
SCF	=	Slat-Cove Filler
SGF	=	Slat-Gap Filler
SPL	=	Sound Pressure Level, dB
WUSS	=	Wing Under Slat Surface
x,y,z	=	Cartesian coordinates
α	=	angle of attack, degrees
η	=	normalized spanwise distance
Φ	=	observer angle, degrees
θ_e	=	polar emission angle, degrees

I. Introduction

The NASA Aeronautics Research Mission Directorate Advanced Air Transport Technology Project includes as one of its baseline goals the understanding and mitigation of radiated noise from high-lift systems on commercial-class transonic aircraft. Slat noise has been identified as a prominent source of airframe noise during aircraft approach and landing, competing with noise generated by trailing-edge flaps and the aircraft undercarriage [1–8].

The reduction of slat noise requires a synergistic experimental assessment of the baseline noise generated by unmodified slat structures, coupled with high-fidelity numerical simulations of the flow-induced noise mechanisms on these structures. An understanding of the noise generation mechanisms can then drive the development and deployment of practical and effective noise mitigation concepts. Over the past two decades, a number of experimental and computational studies have been performed to understand and model the noise generated by leading-edge slats (for a generic geometry see Fig. 1) [9–13].

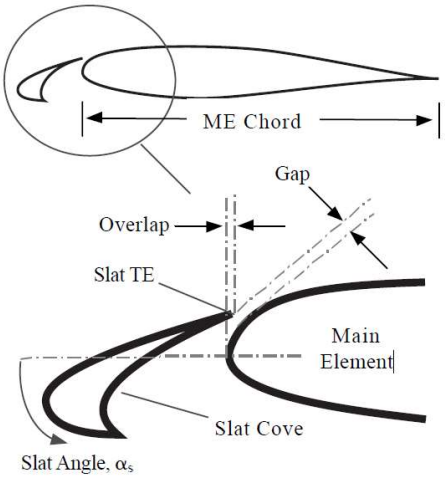

Fig. 1 Generic leading-edge slat geometry (from Ref. 13).

Previous measurements by Moriarty et al. [14] have shown the flow through the slat gap to be at a much higher speed than the freestream flow. Moriarty also found the highest turbulent kinetic energy levels in the slat-gap region, where reattachment of the separated shear layer occurs. These experimental findings have been confirmed via computational studies such as those presented for a two-dimensional high-lift 30P30N model at the 2014 Workshop on Benchmark Problems for Airframe Noise Computations (BANC-III) [15]. The computational predictions and measurement data suggest the slat-gap flow to be a dominant source of radiated noise, and imply that modification of the flow through the gap could be an effective way of mitigating slat noise. This was demonstrated by Zhang et al. where the incorporation of a gap filler was found to yield a 10 dB reduction in broadband slat noise in comparison with the baseline [16]. Recently, Yamamoto et al. have demonstrated a method of slat noise reduction by extending the slat chord near the trailing edge and by attaching a bump on the slat lower surface, resulting again in 10 dB reductions in broadband slat noise [17].

The goal of the current study was to demonstrate slat noise reduction on a high-fidelity model of a commercial transport-class aircraft. This was performed using an instrumented, 10%-scale, semispan High-Lift Common Research Model (CRM-HL) installed in the NASA Langley 14- by 22-Foot Subsonic Tunnel (14x22) in the Fall of 2020. An objective of the wind tunnel campaign was to characterize the nature of baseline and treated slat noise radiation via: (1) assessment of the general aerodynamic performance of the model, (2) identification of noise source regions on the model, (3) quantification of the noise source strengths, (4) measurement of radiated noise directivity, and (5) comparison of experimental data with computational simulations of the noise. The aerodynamic

performance of the model was assessed using a large ensemble of both time-averaged and unsteady surface pressure sensors, with the acquired data compared with computational simulations. The acoustic characterization was conducted using a traversing microphone phased array mounted along the sidewall of the tunnel test section viewing the pressure side of the model. The array and associated traversing mechanism can be seen in Fig. 2 installed in the 14x22 tunnel. A modified version of the DAMAS beamforming and point spread function (PSF) deconvolution code incorporating corrections for shear layer decorrelation [18] was used to obtain noise contour presentations and directivity for acoustic sources present on the model.

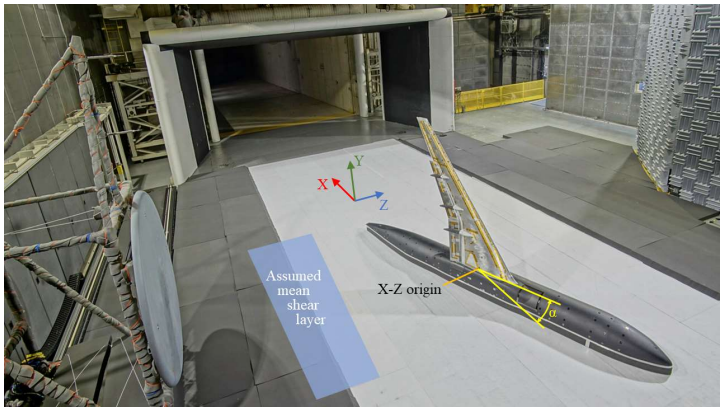

Fig. 2 Phased array viewing pressure side of CRM-HL, looking downstream in the 14x22 tunnel [Source: NASA].

This experimental campaign began when NASA developed a multipurpose CRM-HL model intended for active flow control [19] and aeroacoustic testing. Computational simulations were used to support the model development, provide important information such as load distributions along the high-lift elements, and to aid in the design of noise reduction devices. Commercial CFD Powerflow[1] software, version 5.5b, was used to make aeroacoustic predictions of the noise from the CRM-HL. Powerflow was used extensively during the design of the noise reduction technologies applied to a similarly-sized semispan Gulfstream aircraft model tested in the LaRC 14x22 subsonic tunnel [20], and the noise predictions made before the experimental testing compared very well with the measurements. Therefore, a similar approach was used for the CRM-HL campaign. Initial time-accurate simulations of the flow over the CRM-HL in the landing configuration were completed in 2017 [21], and the mean flow field was shown to be in reasonable agreement with the steady CFD results from the NASA codes. Simulations of both a full-span slat without the engine and a part-span slat with a nacelle/pylon were performed. Surface pressure fluctuations and synthetic microphone array beamform maps were used to identify potential noise sources. More refined simulations [22] were compared with experimental results from a 2018 risk-reduction test in the 14x22

[1] Specific vendor and manufacturer names are explicitly mentioned only to accurately describe the test hardware. The use of vendor and manufacturer names does not imply an endorsement by the U.S. Government nor does it imply that the specified equipment is the best available.

where aerodynamic and acoustic measurements of the baseline model were acquired in a closed, hard-wall test section. Good agreement was obtained for the time-averaged surface pressures, and the acoustic predictions captured the same trends as the microphone array data measured in the closed test section. Subsequently, full-scale, realistic structural designs were developed for noise reduction devices, and the devices then applied to the 10%-scale model. The aerodynamic and aeroacoustic performance was evaluated using unsteady simulations, which also provided detailed load information and guidance on how sensitive the performance was on particular facets of the geometry. This process was iterated until designs were obtained with good structural, aerodynamic, and aeroacoustic performance. The 2020 14x22 test was used to experimentally investigate in an open-jet tunnel configuration the most promising designs, in particular that of a slat-gap filler (SGF) [23, 24]. Based on the confidence in the simulations from the 2018 risk reduction study, only minimal static pressure ports were included on the low-noise slats built for the 2020 test. Hence, simulation data will be shown here to augment the experimental data and fill-in gaps between the measured points.

This paper presents a detailed characterization of the general aerodynamic performance of the model along with measurements of noise radiated by the leading-edge slat for both baseline and noise-treated configurations as obtained during the 2020 14x22 test campaign. Results include aerodynamic lift and pressure coefficient distributions, integrated spectra of noise source regions, and the effects of Mach number, angle of attack, and acoustic source directivity on acoustic radiation. The organization of the paper starts with Section II providing a detailed description of the test campaign. This is followed by Section III describing the computations that were conducted. Section IV discusses briefly the aerodynamic measurements that were obtained followed by an in-depth discussion of the aeroacoustic measurements. Finally, Section V presents an overall summary of the findings from the study.

II. Test Description

A. Open-Jet Wind Tunnel

The 14x22 tunnel (Fig. 3) is an atmospheric, closed-return tunnel that has the capability to test a variety of fixed- and rotary-wing aircraft and test articles, both powered and un-powered. The tunnel has a contraction area ratio of 9:1. Using a 12,000 horsepower drive system, the tunnel can generate airflows up to Mach 0.3, corresponding to a maximum unit Reynolds number of 7.2×10^6 per meter (2.2×10^6 per foot). The test section has

dimensions of 4.4-meters (14.5-feet) high by 6.6-meters (21.75-feet) wide by 15.3-meters (50-feet) long and was configured for partial open-jet (floor in place) operation for the present study. For acoustic testing, the floor of the test section was lowered approximately 0.6 meters (2 feet) to permit the installation of rigid steel frame baskets containing sound-absorbing acoustic foam wedges topped with foam sheets and perforated metal panels. The perforated panels were covered by an adhesive felt layer to reduce floor scrubbing noise (Fig. 2). Additionally, foam sheets were applied to the floors outside of the test section. A combination of acoustic foam wedges and perforated panels were attached to the raised ceiling and outer sidewalls of the test section. When combined with the floor baskets, these treatments created an effective semi-anechoic environment in the open-jet test section that minimized unwanted acoustic reflections. Key dimensions of the open-jet test environment, referenced to the coordinate system shown in Fig. 2, are given in Table 1.

Fig. 3 Aerial view of the 14x22 tunnel [Source: NASA].

A detailed series of empty-tunnel noise measurements were conducted at the conclusion of the CRM-HL test campaign to characterize the background noise levels in the facility as a function of Mach number and array location. A typical ensemble of background noise spectra for the center array microphone at the 90-degree array station (i.e., the flyover location) as a function of tunnel freestream Mach number is shown in Fig. 4. Based on these background levels, the tunnel noise floor for the majority of the spectra shown subsequently in this paper was deemed acceptable. Additional details regarding the background noise characterizations and the noise reduction treatments applied to the tunnel are described by Hutcheson et al. [25].

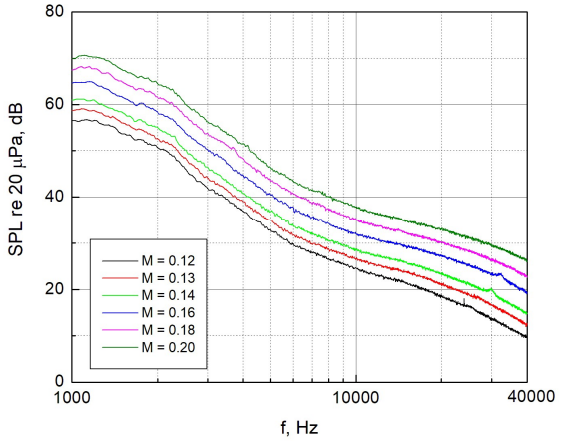

Fig. 4 Tunnel Background Spectra. Array Microphone #1, $\phi = 90^{\circ}$.

Table 1 Key Dimensions of Open-jet Test Section Environment Shown in Fig. 2

Direction	Description	Distance (meters)	Distance (feet)
x	Nozzle exit plane to origin	5.97	19.58
x	Nozzle exit plane to collector	14.48	47.50
y	Origin to upper shear layer centerline	4.42	14.50
y	Origin to ceiling wedge tips	6.78	22.25
z	Side shear layer centerline to origin	3.35	11.00
z	Array face to origin	5.17	16.96
z	Array sidewall to origin	6.71	22.00
z	Origin to far sidewall	14.63	48.00

B. Common Research Model

1. Baseline Model

The baseline model tested for this study was a 10%-scale version of the CRM-HL developed by Lacy and Sclafani [26] with a 2.9-meter (9.7-foot) semispan and a 0.7-meter (2.3-foot) mean aerodynamic chord. The model represented an open geometry and consisted of a supercritical transonic wing with a fuselage representative of a widebody commercial transport vehicle. The full model was comprised of a fuselage, wing, inboard and outboard trailing-edge flaps, inboard and outboard leading-edge slats, a pylon and flow-through nacelle, and a high-fidelity main landing gear. Two slat configurations were available for testing: (1) a full-span slat (FSS, Fig. 5) where the pylon and nacelle were removed and replaced with a bridge section, and (2) a part-span slat (PSS, Fig. 6) where the pylon and nacelle were in place. For the approach and landing configuration tested here, the flap deflections were set to 37 degrees and the slat deflections were set to 30 degrees. The model geometry included fifteen slat brackets,

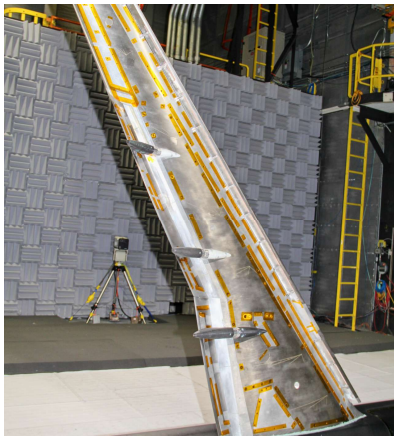

Fig. 5 CRM-HL FSS configuration [Source: NASA].

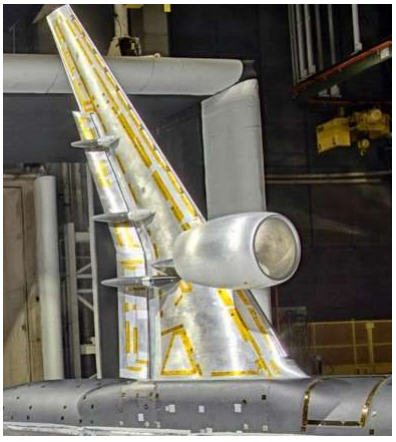

Fig. 6 CRM-HL PSS configuration [Source: NASA].

three flap brackets, and flap track fairings. The slat brackets employed in this investigation were more realistic (in terms of curvature and the location that they emanate from the main element) than those previously tested [24]. The model was heavily instrumented with static pressure taps distributed on the main element, flap and slat, and a number of unsteady pressure transducers situated along the span of the baseline slat and main-element leading edge (Fig. 7). The symbols in Fig. 7 represent the static pressure port locations on the model, and computational planar cuts are indicated by the lines on the wing. The cuts were made with the flaps and slats in the stowed position, so a single plane does not cut through all ports when those elements are deployed. The parameter η is the distance in the spanwise direction normalized by the total semispan length. The flap break occurs at $\eta = 0.37$, and the outboard flap extends to $\eta = 0.72$. More detailed descriptions of the model construction and instrumentation can be found in Refs. [27, 28]. CAD (computer aided design) files of the baseline model can be found in Ref. [29].

2. Noise Treatments

Two slat noise reduction concepts were tested for this study: (1) a slat-gap filler (SGF), and (2) a slat-cove filler (SCF) [23, 24, 30, 31]. These are shown conceptually in Fig. 8. The SGF employs an overleaf concept and sustains the local aerodynamic loading when deployed. In contrast, the SCF guides the flow through the slat gap, thereby maintaining baseline high-lift performance while reducing flow unsteadiness and associated noise. The development of these noise reduction devices is part of a larger effort within NASA to enable practical applications of reconfigurable aerospace vehicles through the use of shape-memory-alloy (SMA) materials. Many studies [16] have found an acoustic benefit to closing the gap between the slat and main element; however, doing so significantly reduces the angle at which the aircraft will stall. The stall conditions are used to define aircraft operating parameters such as the landing speed, so negatively impacting stall is not acceptable.

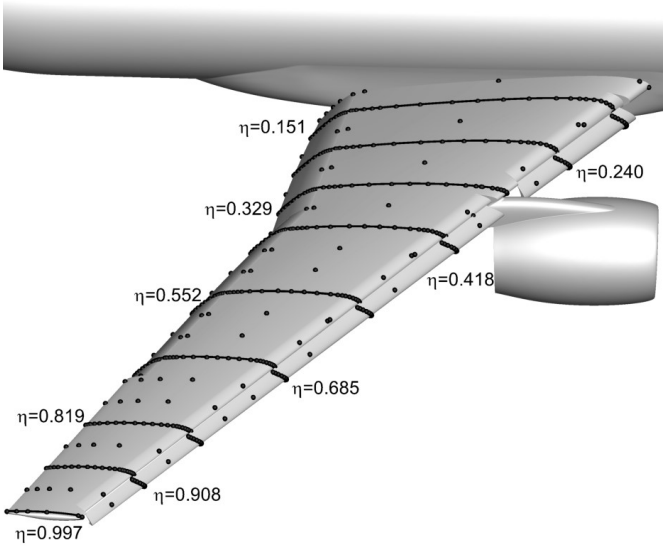

Fig. 7 Static pressure port locations and planar wing cuts used for computational runs. The flap break is at $\eta = 0.37$, and the outboard flap extends to $\eta = 0.72$.

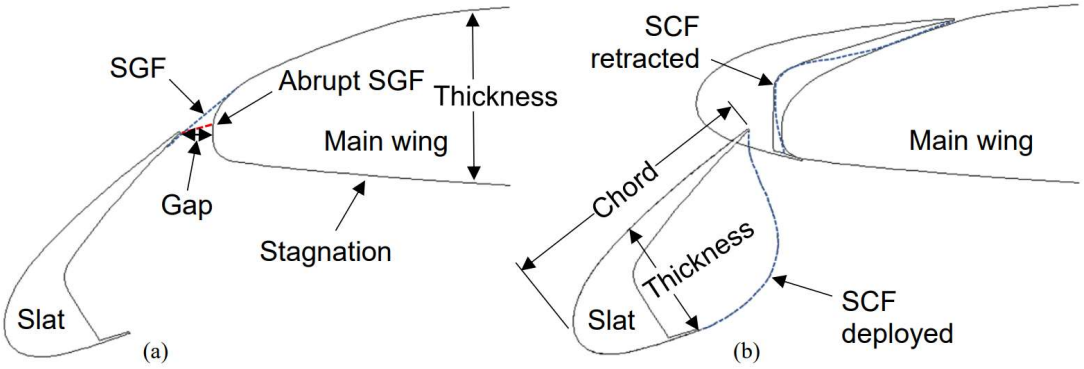

Fig. 8 Schematics of the (a) SGF and (b) SCF concepts (from Ref. 24 – NASA).

However, through the use of SMAs, a thin reconfigurable element has been developed [23, 24] that will close the gap under normal operating conditions but rapidly open the gap when the angle of attack exceeds the expected landing angle by a sufficient margin. Although the noise would be higher when the plane lands with the gap open, this would only occur on the rare occasion when a high angle of attack is encountered. The SGF applied to the CRM-HL was produced with dynamically-scaled thicknesses of nickel-titanium SMA materials and was made to allow the slat to articulate, although such movement was not possible on the wind-tunnel model for this study. Separate structural tests were used to evaluate the behavior of the parts during slat deployment and retraction. Other noise reduction devices were evaluated in the 2018 test described in Section I, and they were also designed to be structurally feasible to implement at full scale and dynamically-scaled for the CRM-HL.

Note that only data obtained using the SGF concept are presented here, with a photo of the installed SGF hardware shown in Fig. 9. Baseline FSS and PSS configurations with and without a SGF and main landing gear (MLG) were tested as part of the wind tunnel campaign. A subset of these is presented in this paper and summarized in Table 2.

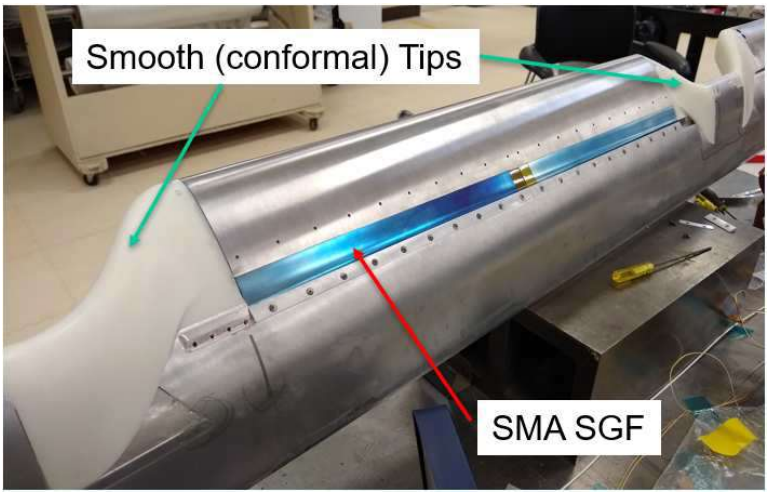

Fig. 9 View of the SGF installed on the model [Source: NASA].

Table 2 Model Configurations Presented in Paper

Configuration #	Full-span Slat (FSS)	Part-span Slat w/Nacelle (PSS)	Slat-Gap Filler (SGF)	Main Landing Gear (MLG)
1	X			
2		X		
3	X		X	
4		X	X	
5	X		X	X
6		X	X	X

C. Phased Array

The phased array incorporated 97 Brüel and Kjær (B&K) Model 4938 6.35-mm (1/4-inch) pressure-field microphones attached to Model 2670 6.35-mm (1/4-inch) preamplifiers powered by B&K NEXUS® 2690 four-channel conditioning supplies. Microphone signals were transmitted to the data acquisition system in the tunnel control room via LEMO microphone cables. The microphones were flush mounted (gap free) in a flat fiberglass honeycomb plate with total diameter of 2.45 meters (8.05 feet). The array was designed for an operational frequency range of approximately 1.5 kHz to 80 kHz. This was achieved by using an irregular circular pattern of microphones comprised of 16 array arms with 6 microphones in each arm (Fig. 10). One microphone was positioned in the center of the array. The maximum array aperture size (outermost microphone to outermost microphone) was 2 meters (6.55 feet), yielding a solid collecting angle of 21.1 degrees at a working distance of 5.2 meters (17 feet) from the array face to the center of the test section [32]. The array was attached to a rigid aluminum mounting frame that was in turn mounted to two parallel 13.4-meter (44–foot) linear traversing rails on the "south" side of the test section (see Fig. 2). The linear rails permitted the array face to traverse the majority of the length of the test section.

D. Data Acquisition

A highly distributed data acquisition system using commercially available hardware was assembled for the phased array. The data system had a total capacity of 128 channels and provided signal conditioning and digitization

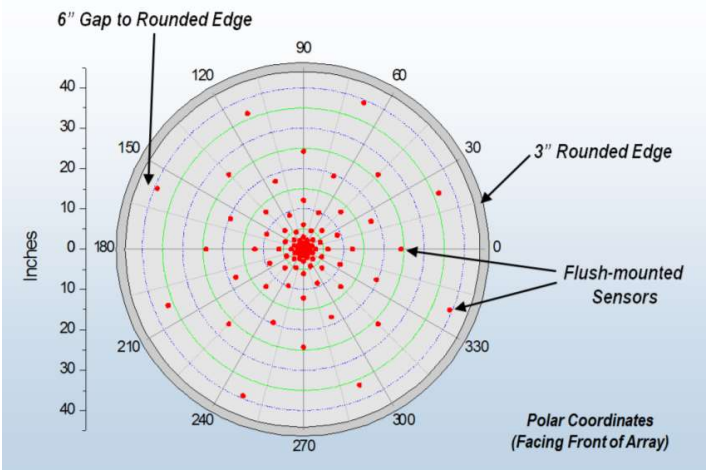

Fig. 10 14x22 traversing phased array geometry.

for both the phased array microphones and auxiliary channels (accelerometers, generated waveforms, and synchronization signals). Signal conditioning was provided by a Precision Filter 68000 system that provided programmable amplification and bandpass filtering. A custom digitization system based on General Standards 24-bit, 64-channel simultaneous sampling PCI cards was constructed and programmed by AVEC, Inc. for the test campaign. A National Instruments LabVIEW®-based program was developed and used for command and control of all the hardware components of the data system as well as the linear traversing rails supporting the phased array. The nominal acquisition window length was 35 seconds with a simultaneous sampling rate of 196.608 kHz for all channels. The microphone signals were bandpass filtered from 1 – 60 kHz. Acquired microphone and auxiliary channel time history data were stored as a series of ensemble raw binary data files coupled with metadata companion files. These were subsequently converted into Hierarchical Data Format Version 5 (HDF5) files for long-term archiving [33].

The static pressure ports on the model were sampled at 10 Hz over an 8-second sampling window using an electronically scanned pressure system, with the outputs of the sensors electronically multiplexed through a single instrumentation amplifier. The pressure system provided automatic calibration of the static pressure ports using a common calibration pressure port. The data for the unsteady pressure sensors on the model were acquired using a 14x22 open architecture dynamic data acquisition system. The simultaneous sampling rate for each unsteady pressure channel was 50 kHz using 24 bits over a 20-second sampling window. A maximum bandwidth of 20 kHz was achieved using bandpass filtering from 0.5 to 20 kHz.

E. Data Reduction and Analysis

1. Phased Array

The reduction of data obtained from the array microphones consisted of several steps. Only brief descriptions of the data reduction steps are presented here. More detailed information can be obtained via the references in this section.

1. For each test point, a Cross-Spectral Matrix (CSM) was generated in engineering units. A subspace background subtraction technique implemented by Bahr et al. [34] and based on eigenvalue decomposition of background noise CSMs was used to remove tunnel circuit noise from the array spectral measurements. An optimized CSM diagonal modification was also employed [35] to remove microphone self-noise from the

measurements, though this was found to have minimal influence on the results when used in conjunction with background subtraction.

2. Detailed analysis of the array data was performed using conventional frequency-domain delay-and-sum beamforming. This was coupled with the DAMAS deconvolution algorithm [36] for generation of final noise source map presentations. The DAMAS algorithm was modified by Bahr [18] to correct for randomization of the propagation path through the turbulence of the tunnel open-jet shear layer. This randomization effect results in coherence loss between microphone pairs, reducing the spatial resolution of the array. The correction incorporates a Mutual Coherence Function (MCF) into the DAMAS propagation model. The MCF is measured using pseudo point sources (speakers) embedded at key locations on the pressure side of the CRM-HL wing, with the point source data acquired at similar tunnel conditions for model data runs. A turbulence model is applied to correct for measurement grid locations away from the point sources. The beamforming and iterative relaxation solver portions of DAMAS remain unchanged. An error function-based array shading algorithm was employed to control the beamwidth of the array across the measured frequency range [37]. The modified DAMAS algorithm is referred to as MCF-DAMAS here.

3. Figure 11 shows the spatial regions that were defined around the model in order to compute 1/12th-octave Sound Pressure Level (SPL) integrated spectra for this study. Zone 1 (referred to as the wing region and shown in red in Fig. 11) represents integration of the entire wing region and is used diagnostically to compare test points where the effects of trailing-edge flap, nacelle, and/or landing gear noise are desired. Zone 2 (referred to as the slat region and shown in blue in Fig. 11) represents integration of the leading-edge slat region in isolation and is used diagnostically to compare baseline and treated slat noise. For each of these two zones, the spectral levels were obtained on

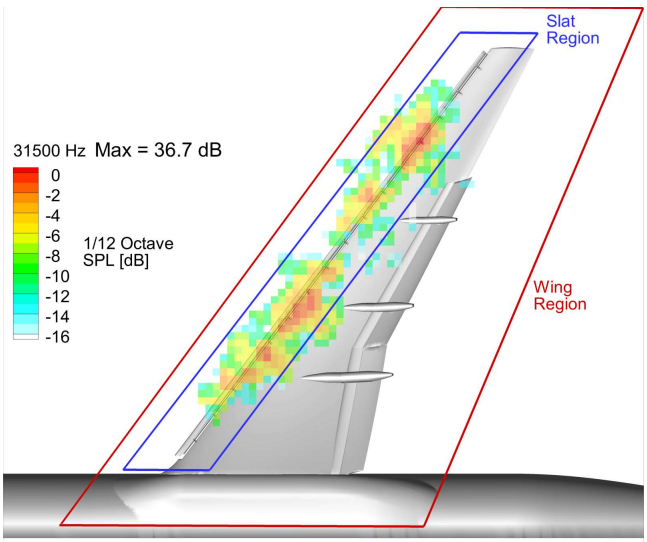

Fig. 11 Source integration regions.

a narrowband basis (Δf = 96 Hz) by simple summing of the mean squared pressures generated by MCF-DAMAS deconvolution over the region(s) of interest. These were then converted to 1/12th-octave bands. All spectral data presented are based on model-scale frequencies. Pressure doubling due to flush mounting of the array microphones has been removed and ray path distance corrections for the various array observer locations are included. It is noted that the wing and slat region integrated spectra for the CRM-HL are similar as almost all of the strong sources occur in the slat region.

2. Pressure Sensors

The electronically scanned static pressure data were post-processed using the 14x22 data system to obtain time-averaged coefficients of pressure. The unsteady pressure data were post-processed to obtain averaged power spectral densities (PSD) of the acquired time series using a periodogram method. A Fast Fourier Transform block length of 5000 points was used with a total of 200 blocks averaged to form the PSDs..

III. Computations

As introduced in Section I, companion numerical simulations were performed using the commercial CFD software Powerflow, a compressible flow solver based originally on a three-dimensional 19 state (D3Q19) Lattice Boltzmann Model (LBM) [38 – 43]. Extensions of the scheme [44, 45] recover a fully compressible form of the unsteady Navier-Stokes equations. Applications of this new version at transonic conditions were presented by Koenig et al. and Fares et al. [46, 47]. All the results presented here were obtained using the high-subsonic option of the baseline solver, which is valid up to Mach 0.9. The solver has been extensively validated for a wide variety of applications over the past 30 years and uses a simpler and more general physics formulation at the mesoscopic level [43]. The Powerflow code can be used to solve the Lattice-Boltzmann equation in a DNS mode, where all turbulent scales are spatially and temporally resolved. However, for most engineering problems at high Reynolds numbers, only the largest scales containing most of the energy are directly resolved, and the small scales are modeled. The current work used the LBM Very Large Eddy Simulation (VLES) approach described in Ref. [42] with wall-functions employed on viscous boundaries. A schematic of the computational domain is shown in Fig. 12, which shows the outer-rectangular box defining the full volume of the simulation. The lower half of the box was defined as a solid and represented an extended floor of the wind tunnel. The red portion indicated the actual test section of the 14x22, and a no-slip boundary condition was prescribed on the model and this section of the floor, whereas the

remainder of the floor was inviscid. Nonreflecting inflow and outflow conditions were defined on the upper portion of the box. No attempt was made to model the actual test section of the tunnel as a previous study [49, 50] indicated that a small angle of attack correction could be used to match the tunnel conditions without the expense of modeling the details of the test section. The solver utilized embedded Cartesian meshes to solve the Lattice-Boltzmann equation, and these regions were defined using primitive shapes, such as the spheres in Fig. 12, using complex shapes from CAD or extracted from flow features, such as was done to refine the grid around the slat-cove shear layer, or within a certain distance of geometry. The grids were generated automatically within the flow solver using input specifications provided by the user. A planar cut of the grid is shown in Fig. 13(a), which illustrates some of the embedded cartesian model. The close-up around the slat in Fig. 13(b) shows the grid concentration around small geometric features such as trailing edges and in regions of important flow features, such as the slat-

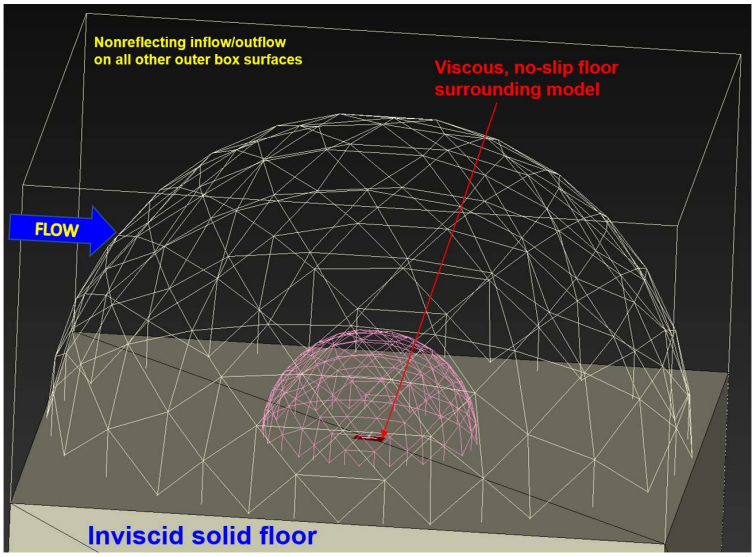

Fig. 12 Computational Domain.

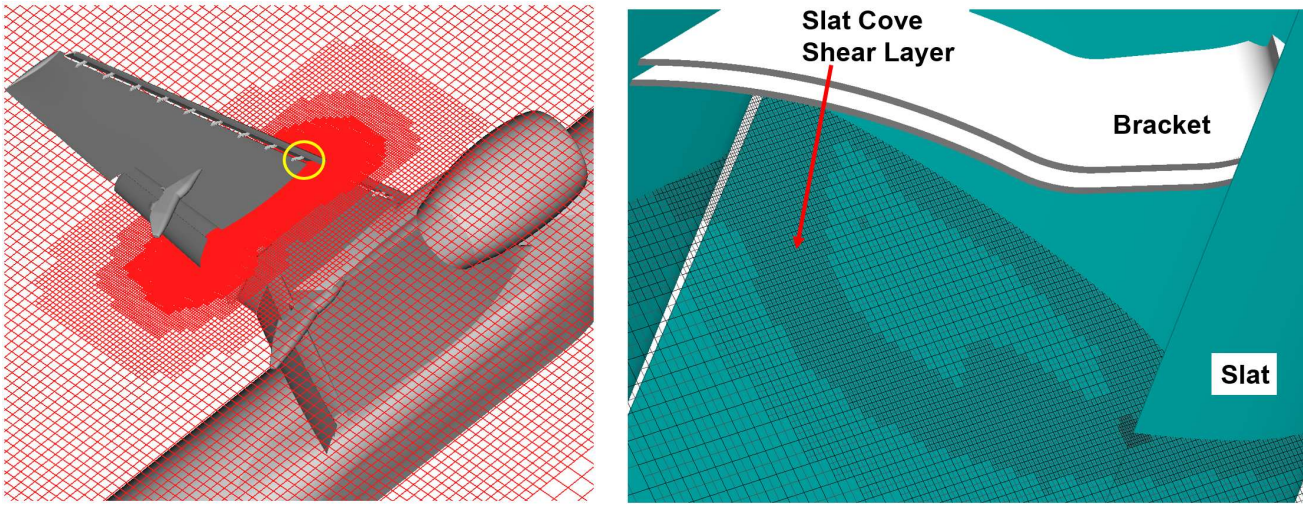

(a) Grid Near Model

(b) Grid in Slat Cove

Fig. 13 Computational Grids around the CRM-HL.

cove shear layer. The smallest spacing of 0.144 mm (0.00567 in, 0.02% of the MAC) was employed around the trailing edges resulting in a total voxel (cell) count of 1.3 billion for the PSS and 1.1 billion for the FSS. The grid sizes were based on a grid resolution study performed in Ref. [22]. The explicit time advancement scheme within Powerflow updated the solution in each cell only when needed, as determined on the basis of the cell size. Only the smallest cells were updated every time step, which was 0.215 microsecond in the current simulations. The calculations were run for 0.55 seconds of physical time with data collection occurring over the last 0.4 seconds when the flow was deemed to be statistically stationary. The simulations were run in a fully turbulent mode at landing conditions (flaps and slats deployed) with a Mach number of 0.20, a Reynolds number (based on the mean aerodynamic chord of 0.7 m (27.58 in)) of 3.27×10^6, and an angle of attack of 8 degrees. The Reynolds number corresponded to the conditions for the 10% model as tested at Mach 0.2 in the 14x22 tunnel. Simulation results for 4- and 12-degree angles of attack were found to be in good agreement with closed-wall experimental data in Ref. [22], and similar comparisons were obtained for the open-jet experiment. However, only results for the baseline landing angle of 8 degrees are presented here. Based on the results of the legacy Gulfstream model testing described in Section I, the pressure distributions from the free-air simulations were expected to match with uncorrected measurements, but at a slightly different angle of attack. Given that the simulations with a free-air configuration above the semispan model should match better with an aircraft in flight than a model in a confined tunnel, the computed C_p values were considered as the reference. The equivalent landing angles of attack of the 2018 closed-test-section and 2020 open-jet measurements were obtained by matching their pressure distributions with the computations at 8 degrees.

In this paper, time-averaged coefficients of pressure, C_p, on the upper and lower surfaces of the model wing were extracted from the simulation results for Configurations 1 through 4 in Table 2. The high-subsonic extension of the LBM used in the simulations was well suited for generating the simulated C_p data for the CRM-HL configurations examined for this study [49, 50]. The reader is referred to Ref. [51] for additional details on the generation of the computed C_p data.

IV. Results and Discussion

A. Aerodynamic Performance

1. Lift Characteristics

When modifying airframe structures to incorporate noise reduction concepts and treatments, an important assessment is validation that the treatments do not adversely affect the aerodynamic performance of the model. Thus, multiple measurements were conducted to ascertain that the installation of SGF components on the CRM-HL did not affect the lift characteristics of the model over the angle of attack range where the gap was expected to be closed. The SGF was designed to quickly retract and open the gap when the angle-of-attack exceeds the landing angle by more than four degrees [24]. The results of these measurements can be seen in Fig. 14 where the coefficient of lift is depicted as a function of the angle of attack α extending from 0 degrees to 20 degrees (representing stall). The data, uncorrected for tunnel confinement effects, were acquired at M = 0.18 with three baseline runs shown (representing Configuration 2, PSS). Excellent repeatability of the lift data was demonstrated from these measurements. The lift characteristics with the addition of the SGF to the model (Configuration 4) are depicted by the blue and magenta triangle symbols and lines in the figure. There was virtually no difference in lift characteristics over α sweeps from 4 – 13 degrees between the baseline and treated model configurations where the flow through the slat gap was eliminated. This verified the correct aerodynamic performance of the model.

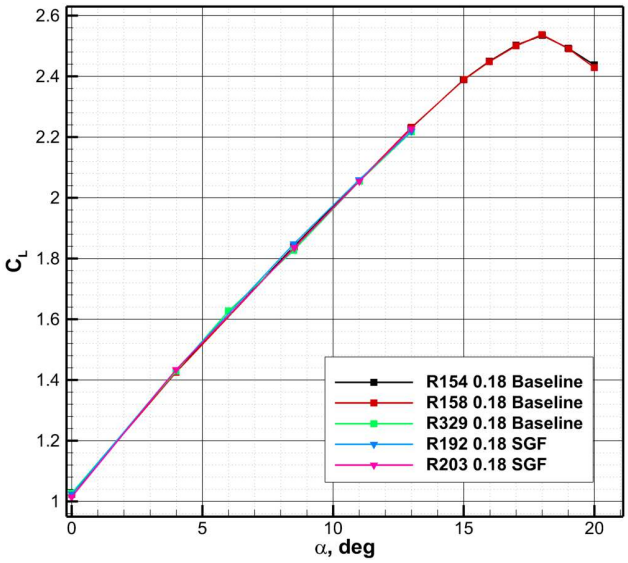

Fig. 14 Coefficient of lift versus angle of attack for baseline (Configuration 2) and treated (Configuration 4) CRM-HL. M = 0.18.

2. Time-averaged surface pressure distributions

Comparisons of measured and computed surface pressures along the selected planar cuts of Fig. 7 are shown in Figs. 15 and 16 for the baseline FSS and PSS (Configurations 1 and 2), respectively. The measured data are uncorrected for any wind tunnel confinement effects. The most inboard cut at η = 0.151 is shown in panel (a) in each figure with the most outboard cut at η = 0.997 shown in panel (f).

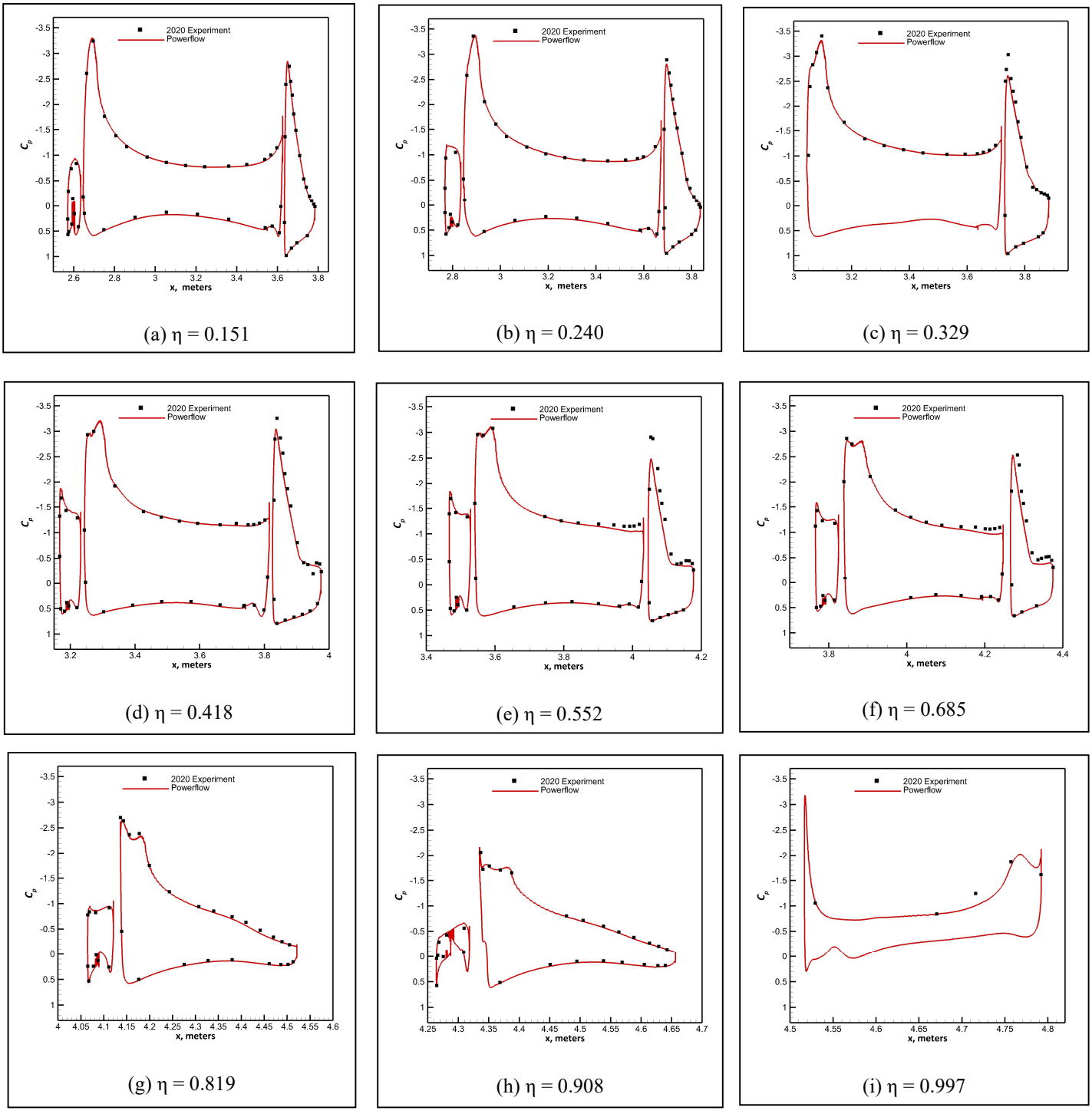

Fig. 15 Surface C_p distributions along cuts for the baseline FSS (Configuration 1). $\alpha = 8.5^{o}$ for experimental data and 8^{o} for simulations. M = 0.2.

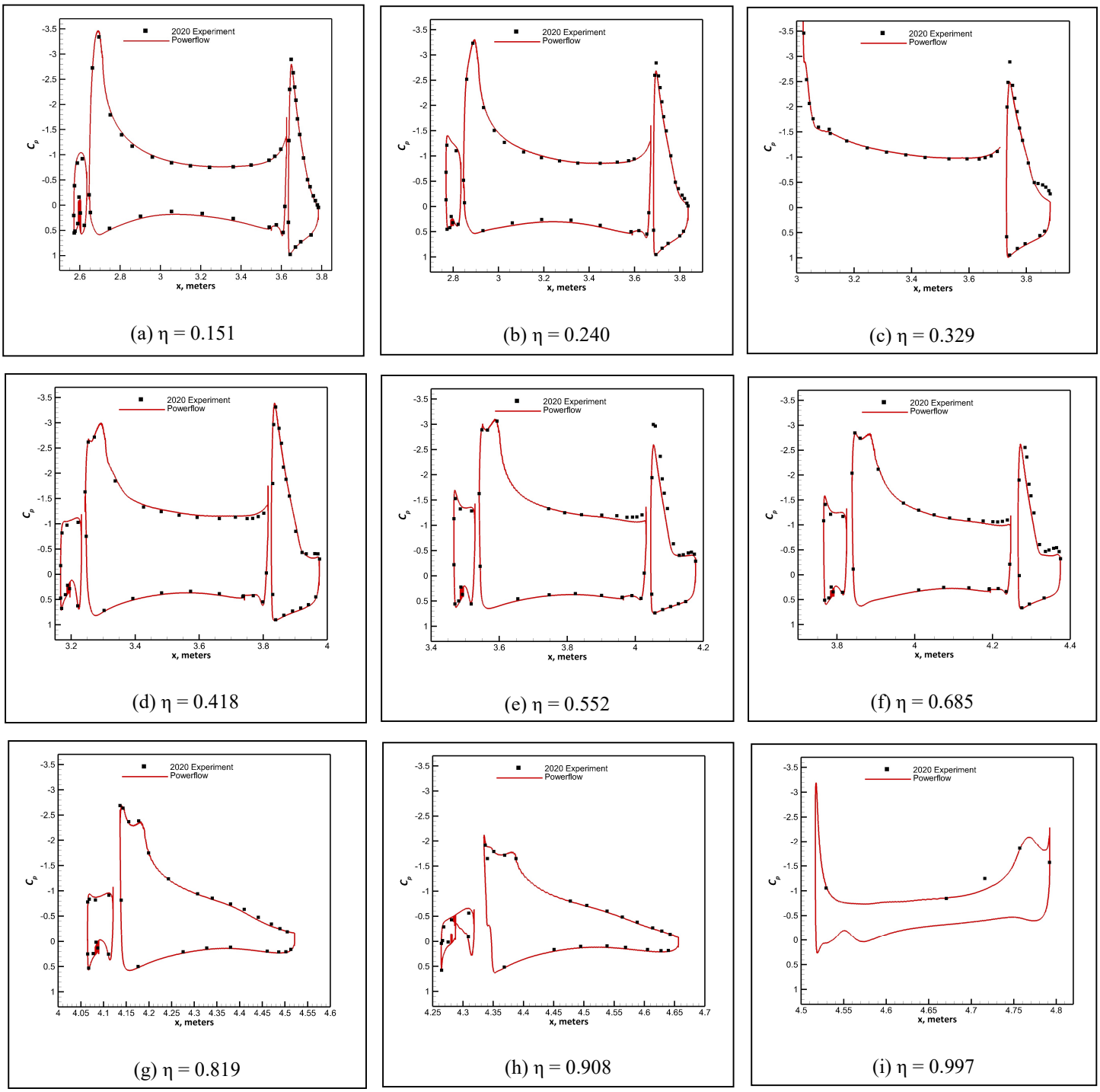

Fig. 16 Surface C_p distributions along cuts for the baseline PSS (Configuration 2). α = 8.5° for experimental data and 8° for simulations. M = 0.2.

To avoid overlapping lines across different elements of the high-lift configuration, the *x* locations of the slat have been shifted upstream by 0.03 m (1.18 in) and the flap downstream by 0.02 m (0.787 in). In general, the agreement between experiment and computation is good at all spanwise stations, but the suction peak on the flap is underpredicted at several locations. Some discrepancies in the details of the separated region on the flap were evident, in particular downstream of the pylon at $\eta = 0.329$ in Figs. 15 and 16. The pressure distribution in the separated region on the flap was sensitive to the grid resolution, and the refinement on the flap was stopped once the distributions on the other elements became relatively insensitive to the grid around the flap. The free-air computations with the semispan model mounted on a viscous floor were run with a value of $\alpha = 8^\circ$, which was the landing angle of attack prescribed in the original definition of the design [26]. The computed surface pressure distributions matched best with the uncorrected pressures from the 2018 closed-test-section measurements [22] at $\alpha = 7^\circ$. The angle of attack for this open-jet experimental study was varied to obtain the best agreement in the surface pressure distributions with the previous closed-test-section measurements, occurring at $\alpha = 8.5^\circ$.

Corresponding comparisons between measured and computed surface pressures when the SGF was added to the FSS and PSS (Configurations 3 and 4) are shown in Figs. 17 and 18. Again, the agreement between experiment and computation was generally good at all spanwise stations with only minor discrepancies noted. There was no significant degradation observed in the overall aerodynamic performance due to the addition of the SGF for these configurations, but some of the load on the main element was shifted onto the slat.

3. Unsteady surface pressure distributions

Fifty-four Kulite® unsteady pressure transducers were installed on the slat, slat brackets, and main-element leading-edge WUSS of the model to obtain spectral information. In general, the highest spectral levels were observed on the WUSS in the wake of the brackets, followed by those on the brackets themselves and then the slat. Selected power spectral density (PSD) spectra for sensors near the midspan of the outboard slat are shown in Fig. 19(a) with their locations depicted in Fig. 19(b). The streamwise location of the sensors on the pressure surface of the slat was as close to its trailing edge as structurally possible (because the slat is very thin near the trailing edge), but it was still upstream of where the slat-cove shear layer reattaches. Hence, the levels on the slat were not the highest on the element (according to the Powerflow simulations), whereas those on the WUSS and brackets were spatially close to where their maxima occur for all the sensors on those elements. WUSS sensor 1237 was where the

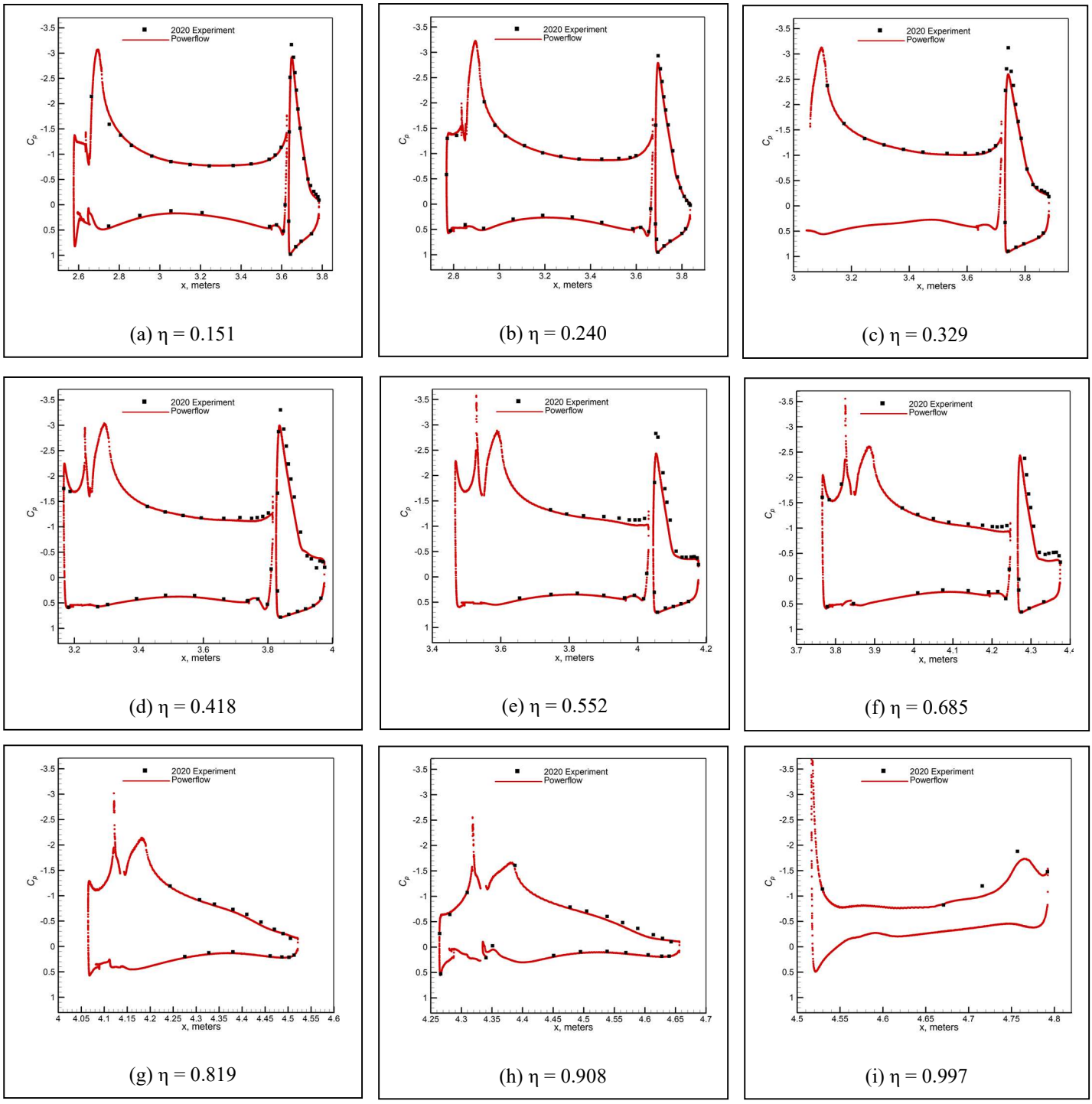

Fig. 17 Surface C_p distributions along cuts for the FSS/SGF (Configuration 3). $\alpha = 8.5^{o}$ for experimental data and 8^{o} for simulations. M = 0.2.

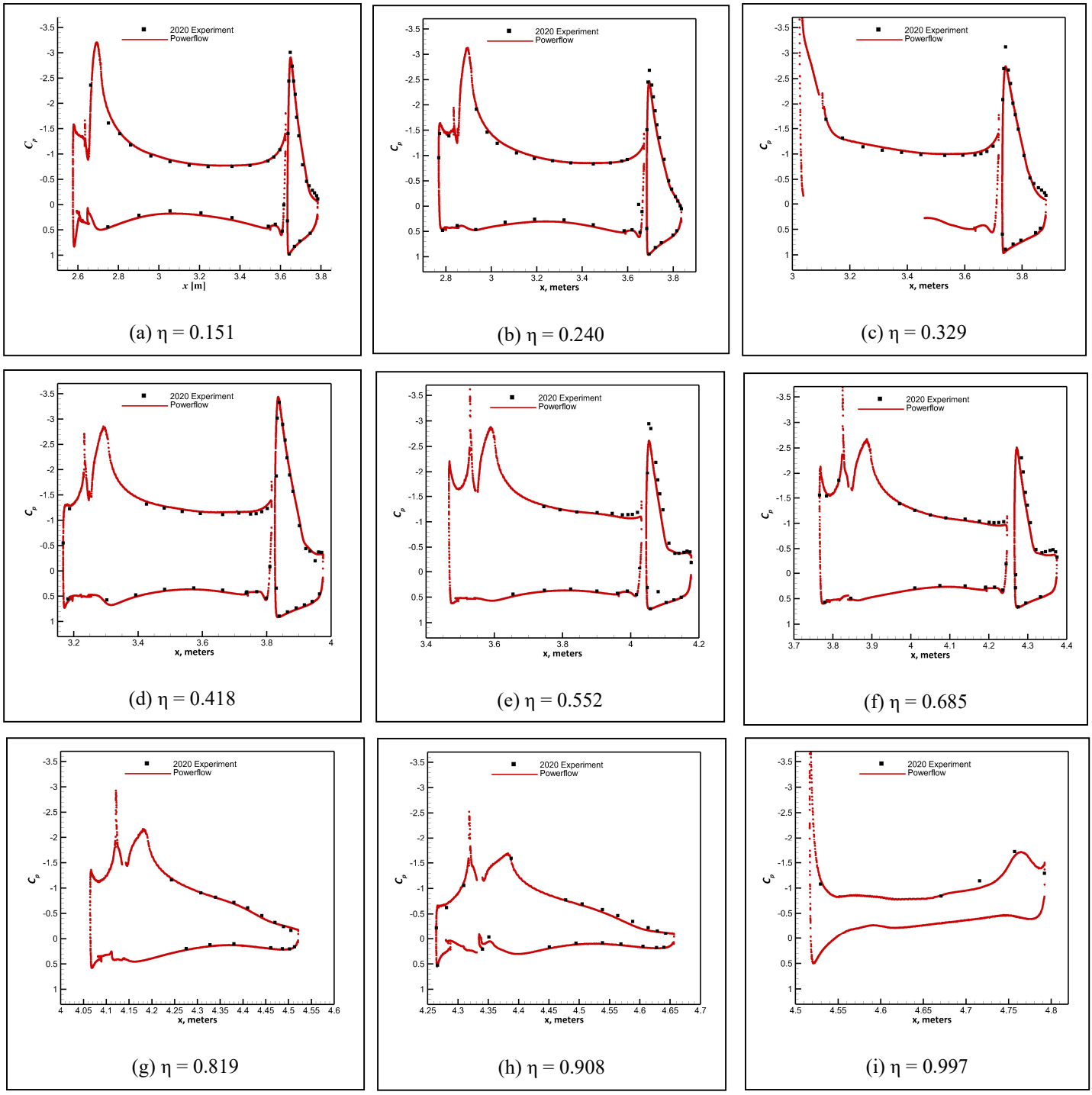

Fig. 18 Surface C_p distributions along cuts for the PSS/SGF (Configuration 4). $\alpha = 8.5^{o}$ for experimental data and 8^{o} for simulations. M = 0.2.

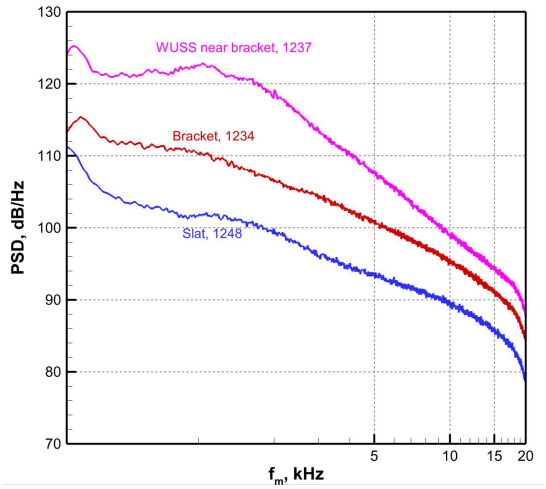

(a) Spectra

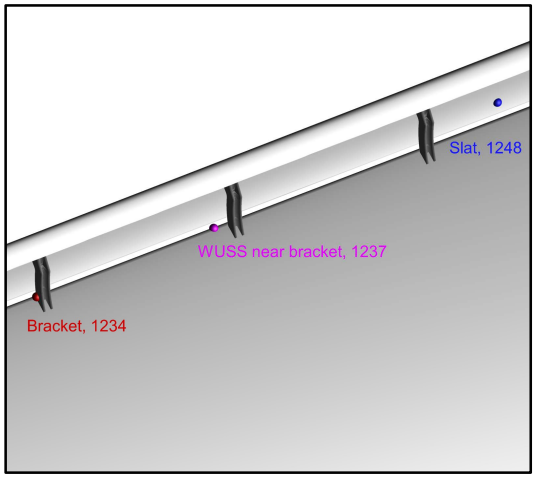

(b) Sensor locations

Fig. 19 Unsteady pressure sensor spectra with high fluctuation levels on the slat, slat brackets, and main-element WUSS for the baseline FSS (Configuration 1). M = 0.2, α = 8.5°

wake from the bracket most impacted the pressure side of the main wing leading edge. This was manifested as a broad energy peak centered around 1 kHz for sensor 1237 in Fig. 19(a).

Figure 20(a) shows spectral levels on the slat at several spanwise locations with the locations of the sensors depicted in Fig. 20(b). These probe locations are placed at the same chordwise location, centered between pairs of adjacent brackets. As such, they were positioned to emphasize the slat-cove dynamics and to gauge the large-scale

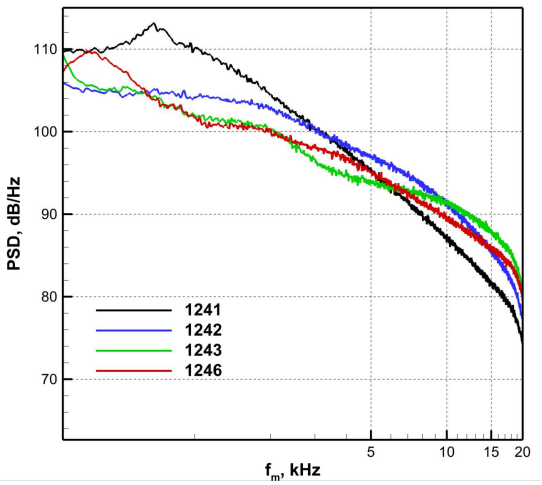

(a) Spectra

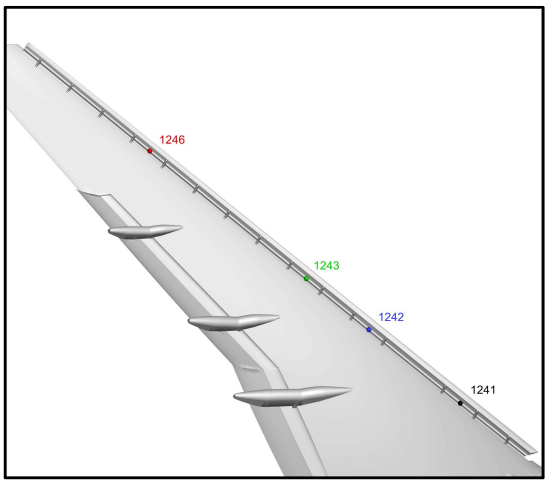

(b) Sensor locations

Fig. 20 Unsteady pressure sensor spectra with the highest levels on the slat for the baseline FSS (Configuration 1). M = 0.2, α = 8.5°

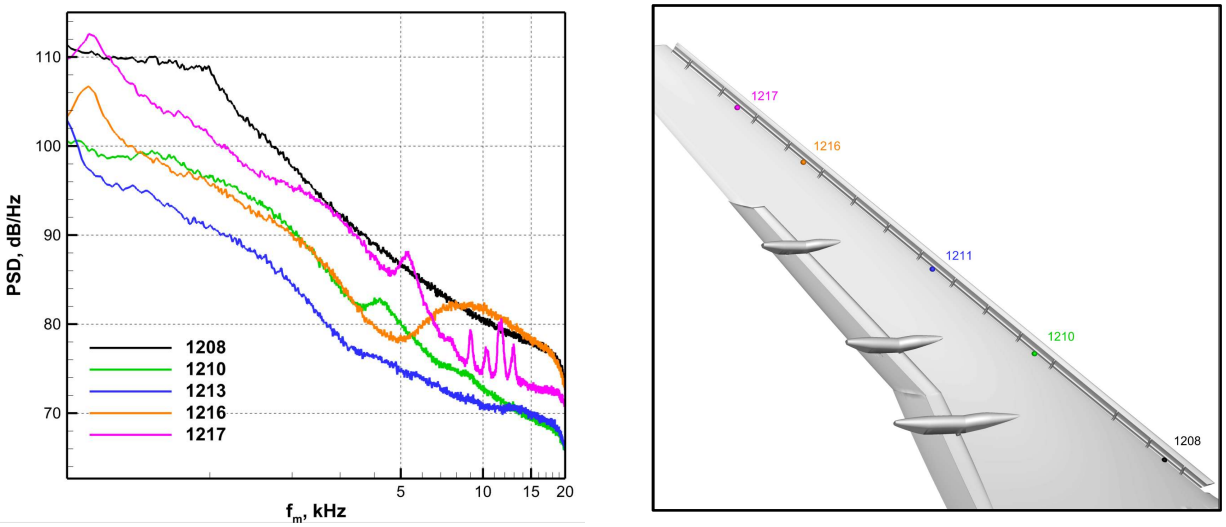

(a) Spectra

(b) Sensor locations

Fig. 21 Unsteady pressure spectra for sensors on the WUSS for the baseline FSS (Configuration 1). M = 0.2, α = 8.5°

trend along the model span. Figure 21(a) shows the spectra for points on the WUSS that were halfway between the slat brackets with the sensor locations depicted in Fig. 21(b). The experimental spectrum for the most outboard point, 1217, exhibited multiple narrow-band peaks typical of low-Reynolds number testing [52]. Point 1216 also exhibited a dramatic rise in levels beyond 5 kHz, and there was a small hump at 4 kHz at point 1210.

B. Acoustic Characterization

Unless otherwise stated, results are shown for a model angle of attack of 8.5 degrees and a Reynolds number of 2.6×10^6 based on the mean aerodynamic chord. The microphone array was positioned at a number of streamwise observer locations with respect to the center of rotation of the model fuselage (the defined reference location on the model). These array stations spanned 70 to 120 degrees in 10-degree increments with an additional station at 56 degrees included in the test matrix (this was the farthest upstream that the array could be traversed). Equivalent polar emission angles were determined from the open-jet shear layer refraction using Amiet's method [53]. All spectra presented in this section were verified for repeatability via examination of at least two identical test points for quality in each case. For brevity, these repeat points are not shown here. Unless otherwise stated, all integrated spectra are computed over the slat region.

1. Baseline Model Geometry – FSS (Configuration 1)

MCF-DAMAS deconvolved source distribution maps are depicted in Fig. 22, showing predominant baseline FSS noise generation regions for a number of 1/12-octave center frequencies spanning 2 – 35 kHz. In each contour presentation, the dB levels have been normalized to the local peak level shown in the map with a total range of 16 dB presented. At lower frequencies, noise radiation from the outer outboard slat region and wing tip dominated, along with contributions from the flap brackets and fairings. Interestingly, at 8 kHz the noise radiation was dominated by a tone-related hot spot occurring in the vicinity of the FSS bridge section. It has been noted [28] that the location of this tone varied with every model configuration and tunnel condition, implying that the conditions needed to produce this resonance are highly dependent on the model geometry and flow. At higher frequencies, the noise radiation was more uniform across the span of the slat region with some individual concentrations of noise observed from a few of the slat brackets. Flap noise was not a significant contributor to the overall noise above 6 kHz.

The effects of angle of attack on the integrated noise spectra for the slat region on the model are shown in Fig. 23. As expected, there was a clear angle-of-attack dependency on the overall spectral levels, with a roughly 5 dB increase observed as α increases from 4 to 13 degrees. It is noted that the spectral shapes observed at all α values were relatively similar with the exception of the observed tones in the 7 to 12 kHz range. There was an observed collapse of the spectra below 1.5 kHz that may have been attributable to prevalent nonslat sources below 2 kHz as well as background noise source effects.

The effect of Mach number variation on the measured noise spectra integrated for the slat region is shown in Fig. 24. While the spectral features were similar at all flow speeds, there was an expected rise in overall SPL as a function of Mach number. Scaling of the Fig. 24 spectra assuming a sixth-power dependency on flow speed is shown in Fig. 25. No Strouhal frequency scaling has been performed. Above 15 kHz, the collapse of the spectra was excellent; however, below approximately 4 - 5 kHz, the collapse appeared to illustrate a fifth-power dependency on flow speed versus a sixth power. The scaling law in the vicinity of the tones was uncertain. It is noted that the tones were resonance phenomena dependent on both geometric and flow characteristics, so frequency and amplitude scaling with speed are unlikely to follow any simple scaling [54, 55].

The effects of observer angle (directivity) on the integrated noise spectra can be seen in Figure 26. Both the physical array observation stations and the equivalent polar emission angles are listed in the figure for reference. At

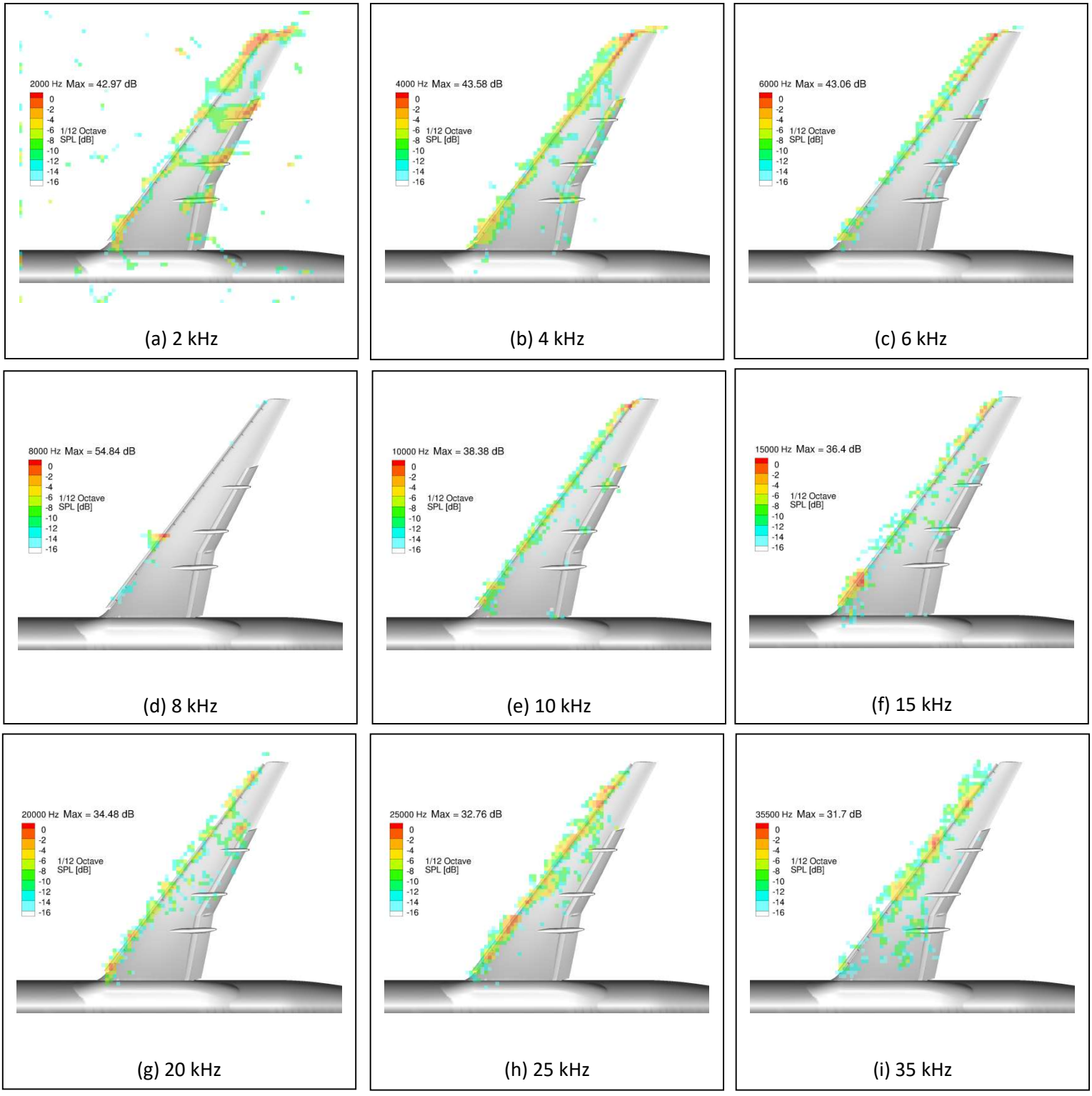

Fig. 22 1/12th-octave band MCF-DAMAS output.
Baseline FSS (Configuration 1), $\alpha = 8.5^{o}$, M = 0.16, $\phi = 90^{o}$.

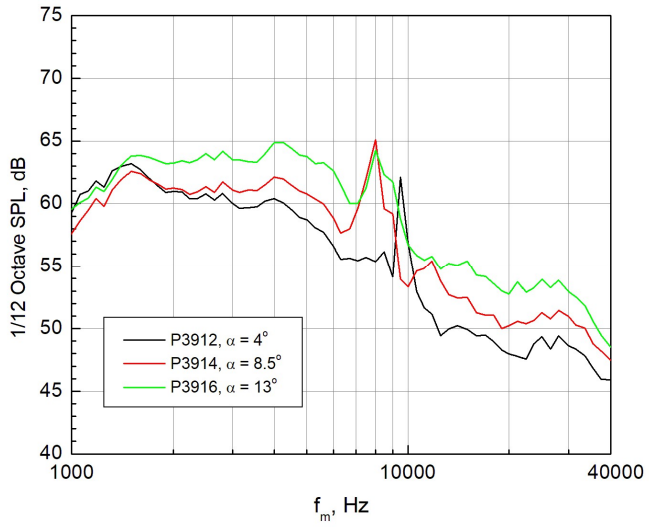

Fig. 23 Baseline FSS (Configuration 1) angle of attack effects. M = 0.16, ϕ = 90º.

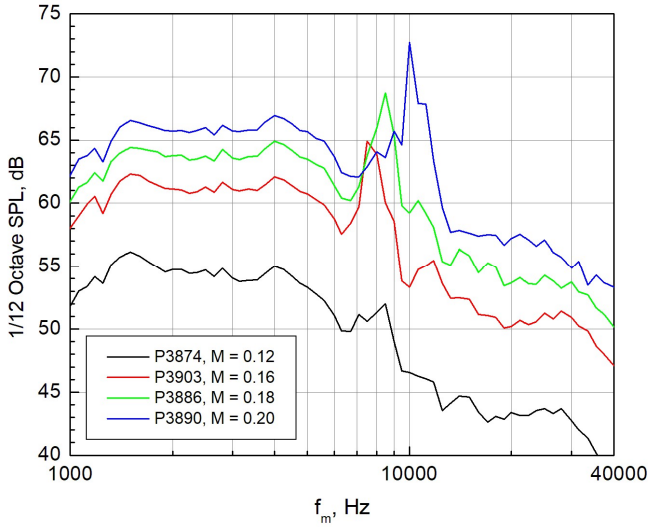

Fig. 24 Baseline FSS (Configuration 1) Mach number effects. α = 8.5º, ϕ = 90º.

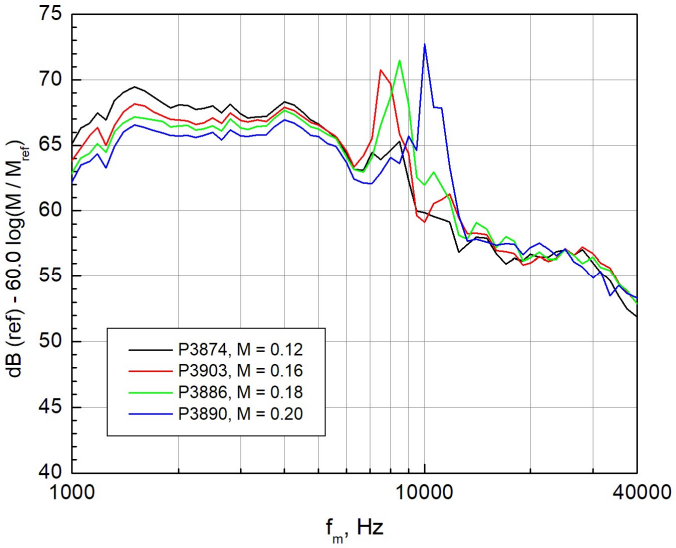

Fig. 25 Baseline FSS (Configuration 1) Mach number scaling. α = 8.5º, ϕ = 90º.

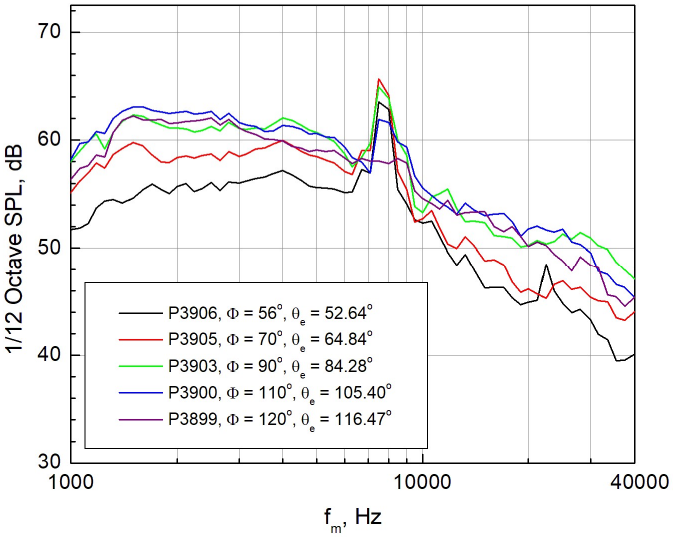

Fig. 26 Baseline FSS (Configuration 1) directivity. α = 8.5º, M = 0.16.

the upstream viewer locations, there were clear decreases in the overall noise level with less variation observed at downstream locations. The structure of the spectra was invariant with observer angle for frequencies away from the 7.5-kHz tonal peaks. Previous investigations of leading-edge slat noise by Mendoza et al. [13] showed omnidirectional source characteristics at lower frequencies; however, this was not observed in the present data, for reasons as yet unknown.

It has been postulated that the baseline slat noise acts as an approximate dipole source. This was investigated for this study by applying a simple dipole scaling function to the directivity spectra, similar to that shown by Mendoza [13]. The spectral normalization takes the form of

$$SPL_{scaled} = SPL - \left[10 * \log\left(\frac{sin^2\theta_e}{(1+M*cos\theta_e)^4}\right)\right] . \quad (1)$$

The application of Equation (1) to the baseline FSS directivity can be seen in Fig. 27. The amplitude scaling utilized the polar emission angles obtained from the tunnel open-jet shear layer refraction, and included dB corrections to account for shear layer ray path differences at the various observer locations. The scaling did an excellent job of collapsing the spectra across the entire frequency range, especially at frequencies below 10 kHz, and confirmed the dipole nature of the radiated slat noise.

2. Baseline Model Geometry – PSS (Configuration 2)

MCF-DAMAS deconvolved source distribution maps are depicted in Fig. 28, showing predominant baseline PSS noise generation regions for a number of 1/12-octave center frequencies spanning 2 – 35 kHz. As in Fig. 22, the dB levels have been normalized to the local peak level given in each map with a 16 dB range shown. At frequencies below 20 kHz, the noise generated in the vicinity of the outboard edge of the inboard slat dominated, likely due to slat bracket and gap flow interactions near the pylon. The noise radiation from this area peaked

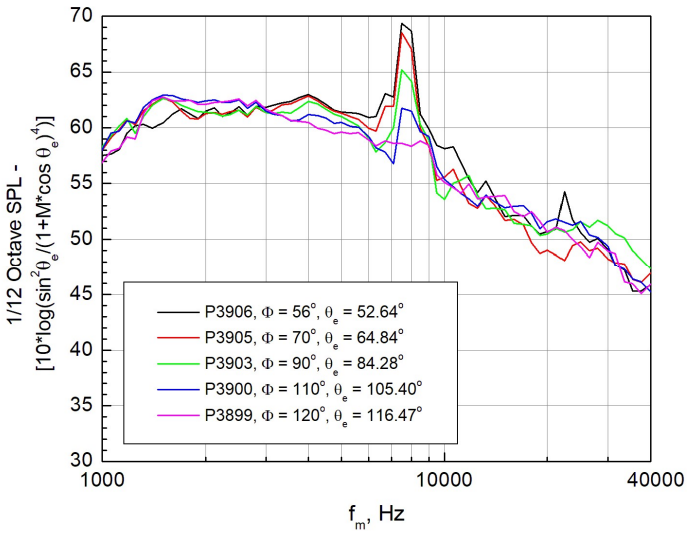

Fig. 27 Baseline FSS (Configuration 1) scaled directivity. α = 8.5°, M = 0.16.

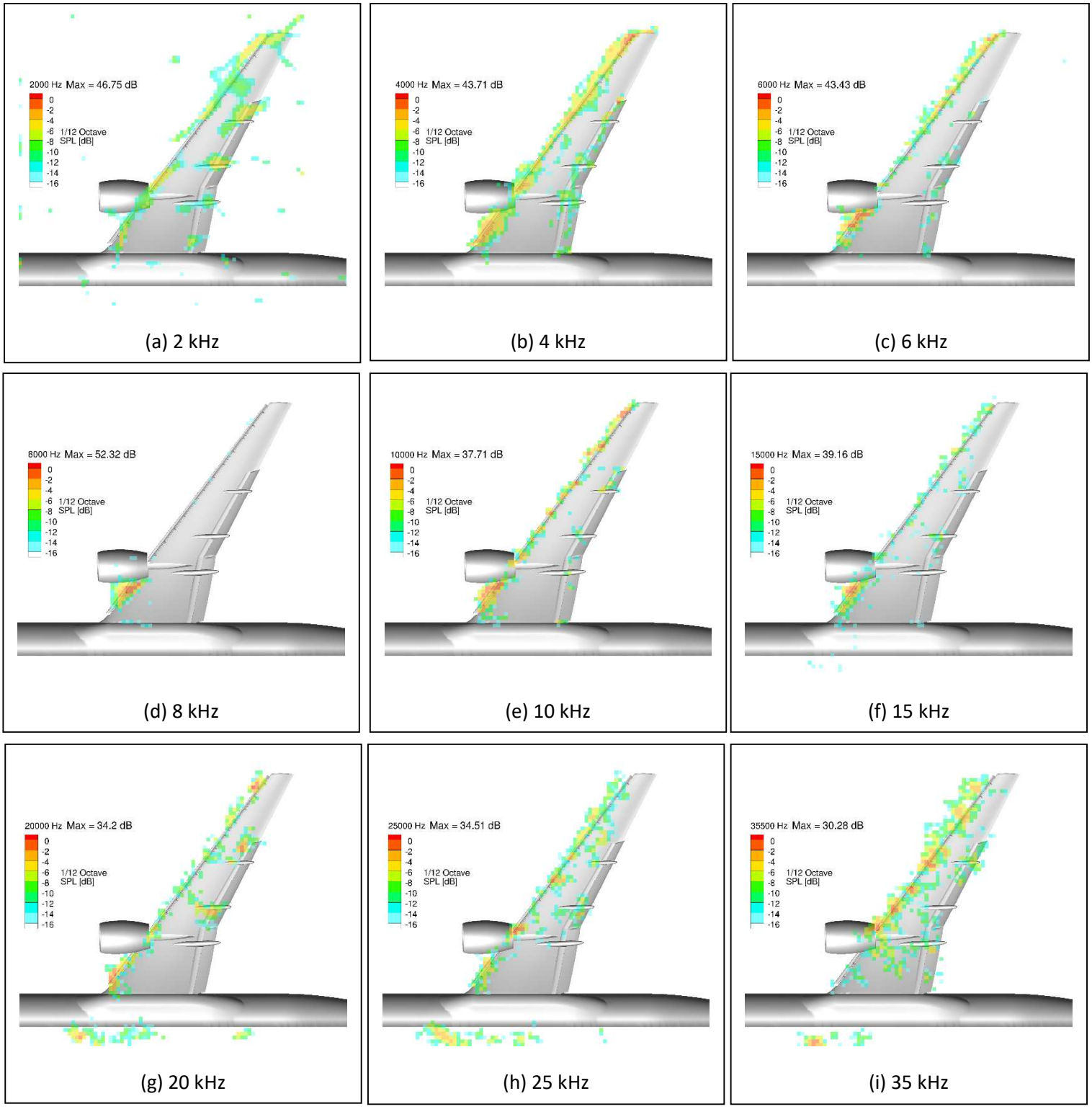

Fig. 28 1/12th-octave band MCF-DAMAS output.
Baseline PSS (Configuration 2), $\alpha = 8.5^{o}$, M = 0.16, $\phi = 90^{o}$.

around 8 kHz and was observed across a range of Mach numbers. Above 20 kHz, the noise was more distributed along the span of the outboard slat, although at 25 kHz a predominant noise source appeared at the inboard edge of the outboard slat near the pylon. Only minimal flap noise was observed at all frequencies. Some noise was observed in the floor region in front of the fuselage above 20 kHz. It is speculated that the source of this noise was a horseshoe vortex interacting with the fuselage and floor when the model was generating significant lift [25]. Subsequent treatment via the application of felt to the offset on the fuselage eliminated this noise source.

The effect of Mach number variation on the baseline PSS measured noise spectra, integrated over the slat region, is shown in Fig. 29. The spectral features below approximately 7 kHz were somewhat similar at all flow speeds. As noted previously, the observed broad tonal features that represent multiple narrow band peaks were produced in the vicinity of the inboard edge of the outboard slat and appeared to approximately adhere to Strouhal scaling from their noted locations in the figure. The observed rise in spectral levels above 20 kHz for the lower Mach numbers matched the observed increase in distributed noise along the span of the outboard slat in Fig. 28. Scaling of the Fig. 29 spectra assuming a sixth-power dependency on flow speed is shown in Fig. 30. Above 15 kHz, the collapse of the spectra was excellent; however, below approximately 4 – 5 kHz, the collapse again appeared to depend more on a fifth power of flow speed versus a sixth power, although the effect was not as pronounced as for the baseline FSS. The velocity scaling law in the vicinity of the tones was again uncertain.

The baseline PSS directivity is represented in Fig. 31 for observer locations spanning 56 to 120 degrees. In general, the addition of the pylon did not appear to significantly affect the directivity for most frequencies, and the spectral variation shown in the figure was remarkably similar to that shown in Fig. 26. The scaled directivity using a dipole assumption and the spectral normalization of Equation (1) is shown in Fig. 32. Below 20 kHz, the collapse of the spectra was excellent confirming dipole behavior; however, there was some residual scatter shown above 20 kHz for currently unknown reasons. It is speculated that tonal noise radiation due to flow interactions around the pylon may have contributed to this variation in dB levels since such radiation could have been directed more to downstream observers.

3. Slat-Gap Filler – FSS (Configuration 3)

It was anticipated that the introduction of a gap filler would significantly reduce the noise generated by the leading-edge slat due to blocking the flow through the gap. This is confirmed in Fig. 33 where MCF-DAMAS deconvolved source distribution maps derived from analyses of the full-span slat with a slat-gap filler were

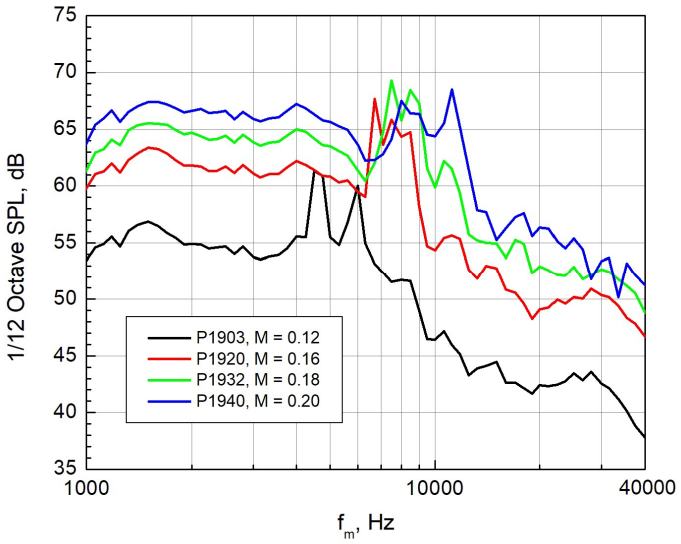

Fig. 29 Baseline PSS (Configuration 2) Mach number effects. α = 8.5°, ϕ = 90°.

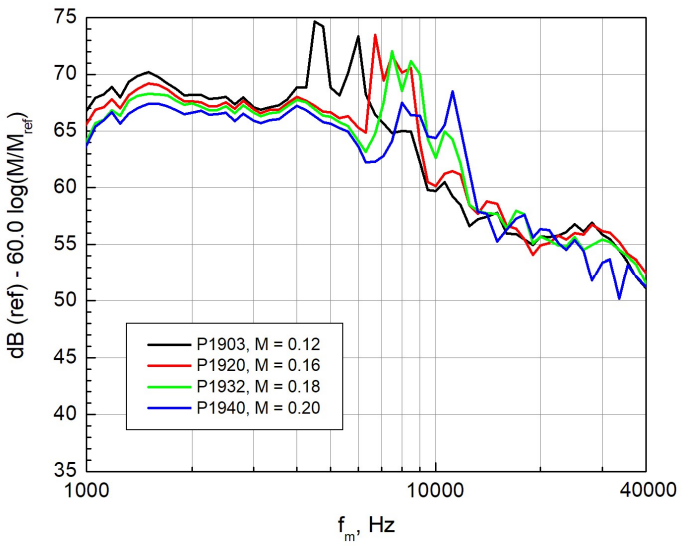

Fig. 30 Baseline PSS (Configuration 2) Mach number scaling. α = 8.5°, ϕ = 90°.

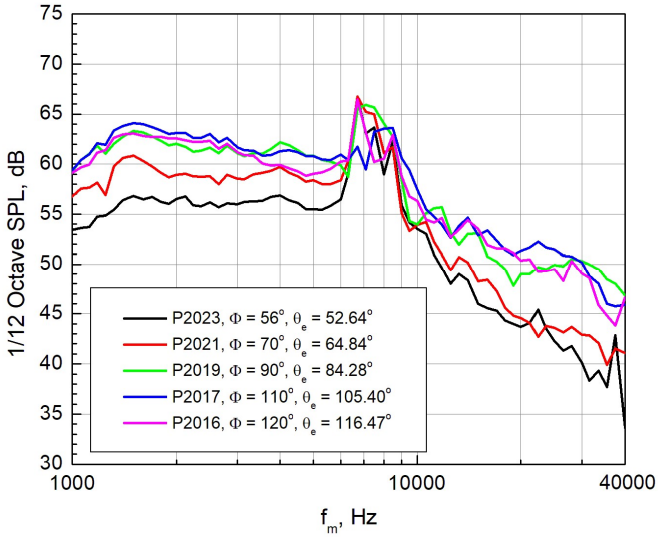

Fig. 31 Baseline PSS (Configuration 2) directivity. α = 8.5°, M = 0.16.

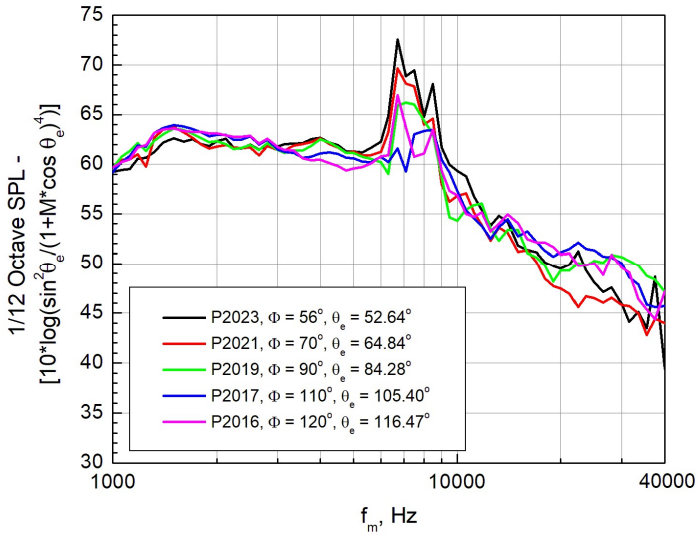

Fig. 32 Baseline PSS (Configuration 2) scaled directivity. α = 8.5°, M = 0.16.

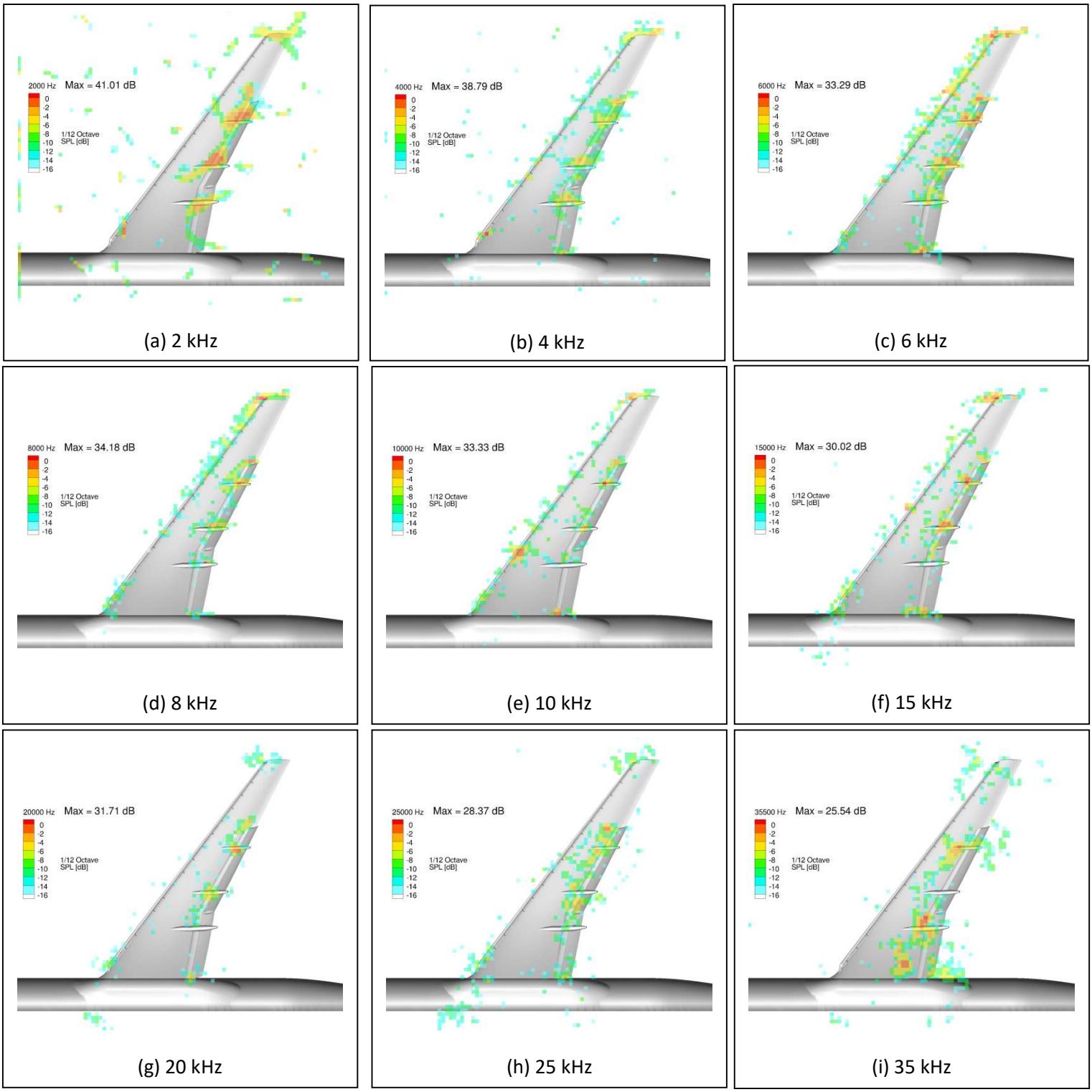

Fig. 33 1/12-octave band MCF-DAMAS output.
FSS with SGF (Configuration 3), $\alpha = 8.5^{o}$, M = 0.16, $\phi = 90^{o}$.

conducted. The model configuration shown in Fig. 33 included full-blockage slat tips in addition to the filler [31]. The slat noise has effectively been eliminated for the majority of 1/12-octave frequencies via the introduction of the gap filler, with the exception of some remaining slat noise at 6 kHz. There was also residual noise observed at the wingtip for a number of lower and mid frequencies. This noise could be a combination of wing-tip vortex noise and outboard slat / slat-tip noise. A small slat tonal spot appeared at 4 kHz with a more prominent one appearing at 10 kHz. These were likely due to flow through a small gap between the tip treatment and the rest of the slat and were later eliminated via application of clay and tape in these regions. With the reduction of the slat noise, the flap noise appeared as a dominant (but still low-level) noise generation mechanism, with outer flap-edge and bracket noise appearing for many of the frequencies.

Figure 34 presents a comparison of the integrated noise spectra for the baseline FSS versus the FSS with the added SGF. Dramatic reductions of up to 10 dB in the spectral levels are shown in the comparison for all observer angles, especially above 3 kHz. The broadband tonal structure occurring around 7.5 kHz for the baseline FSS has been completely eliminated, although a couple of tones appear at approximately 10.6 kHz and 22.4 kHz for the FSS/SGF configuration. Inspection of MCF-DAMAS source distribution maps revealed that the higher-frequency tone emanated from just upstream of the outboard flap bracket, while the lower frequency tone appeared on the slat bridge piece where difficulties were encountered in sealing the ends.

The effect of Mach number scaling on the measured FSS/SGF noise spectra integrated over the slat region is shown in Fig. 35. As with Fig. 25, a sixth-power dependency on flow speed is assumed, resulting in an excellent collapse of the spectra. Curiously, the fifth-power dependency observed for the baseline FSS at lower frequencies did not appear when the SGF was added, although there was a notable deficit in the spectral level at Mach 0.12 for frequencies less than 5 kHz.

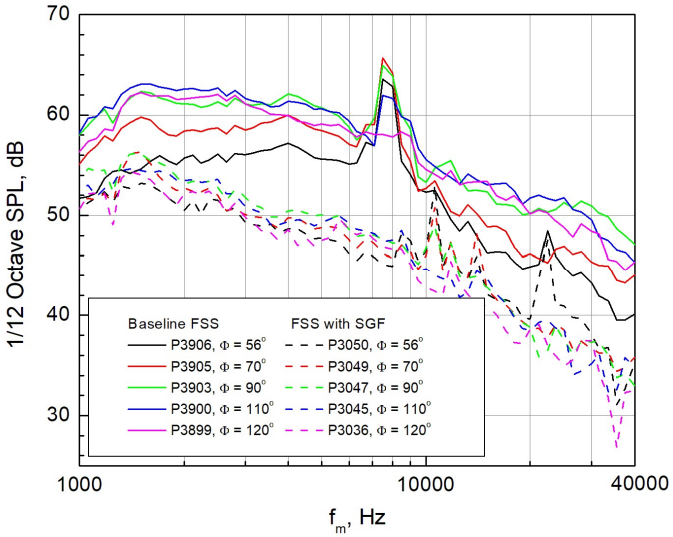

Fig. 34 Comparison of Configurations 1 and 3 (Baseline FSS and FSS with SGF) α = 8.5°, M = 0.16.

It was anticipated that the addition of the SGF would affect the directivity of the slat and this is confirmed in Fig. 36. The dipole directivity observed for the baseline FSS in Fig. 27 has been replaced with approximate omnidirectional noise across the entire frequency span for the FSS/SGF configuration, although there were still some variations as a function of observer angle. In general, lower spectral levels were observed at upstream locations with somewhat higher levels seen at downstream locations. The exception to this was for $\phi = 56^{\circ}$, where the spectral levels at this observer angle relative to the levels at $\phi = 90^{\circ}$ were greater for frequencies above 10 kHz than for frequencies lower than this.

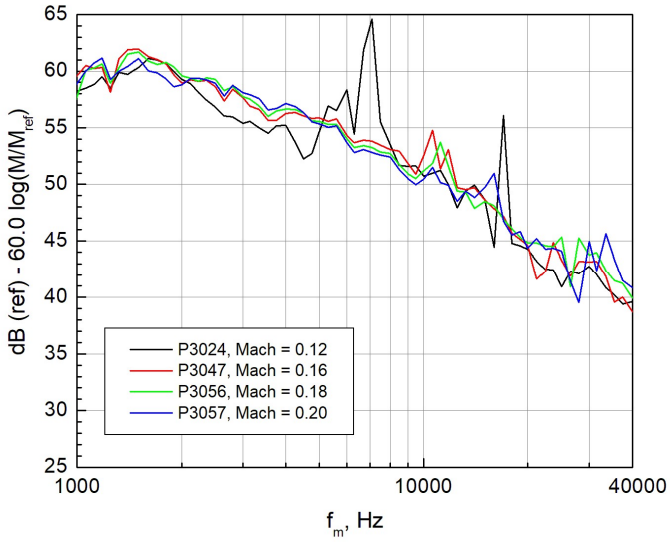

Fig. 35 FSS / SGF (Configuration 3) Mach Number Scaling, $\alpha = 8.5^{o}$, $\phi = 90^{o}$.

4. Slat-Gap Filler – PSS (Configuration 4)

MCF-DAMAS deconvolved source distribution maps for the PSS/SGF configuration are shown in Fig. 37. This model configuration, as described in Section II, included full-blockage slat tips. The introduction of the gap filler again eliminated the majority of slat noise for most of the displayed 1/12-octave frequencies for this configuration, with the exception of some residual noise observed along the outboard slat between 4 and 8 kHz. There was also noise observed at the wingtip between 4 and 20 kHz, as well as a small broadband spot appearing at the aft end of the wing root for frequencies spanning 4 – 25 kHz. Flap backet noise was somewhat more prominent for this configuration versus the FSS/SGF with significant noise observed for the outboard flap bracket at 8 kHz and the midflap

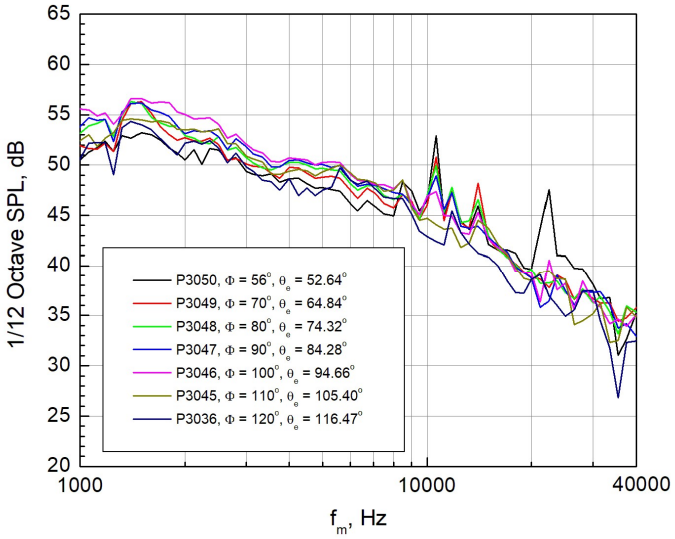

Fig. 36 FSS / SGF (Configuration 3) Directivity, $\alpha = 8.5^{o}$, M = 0.16.

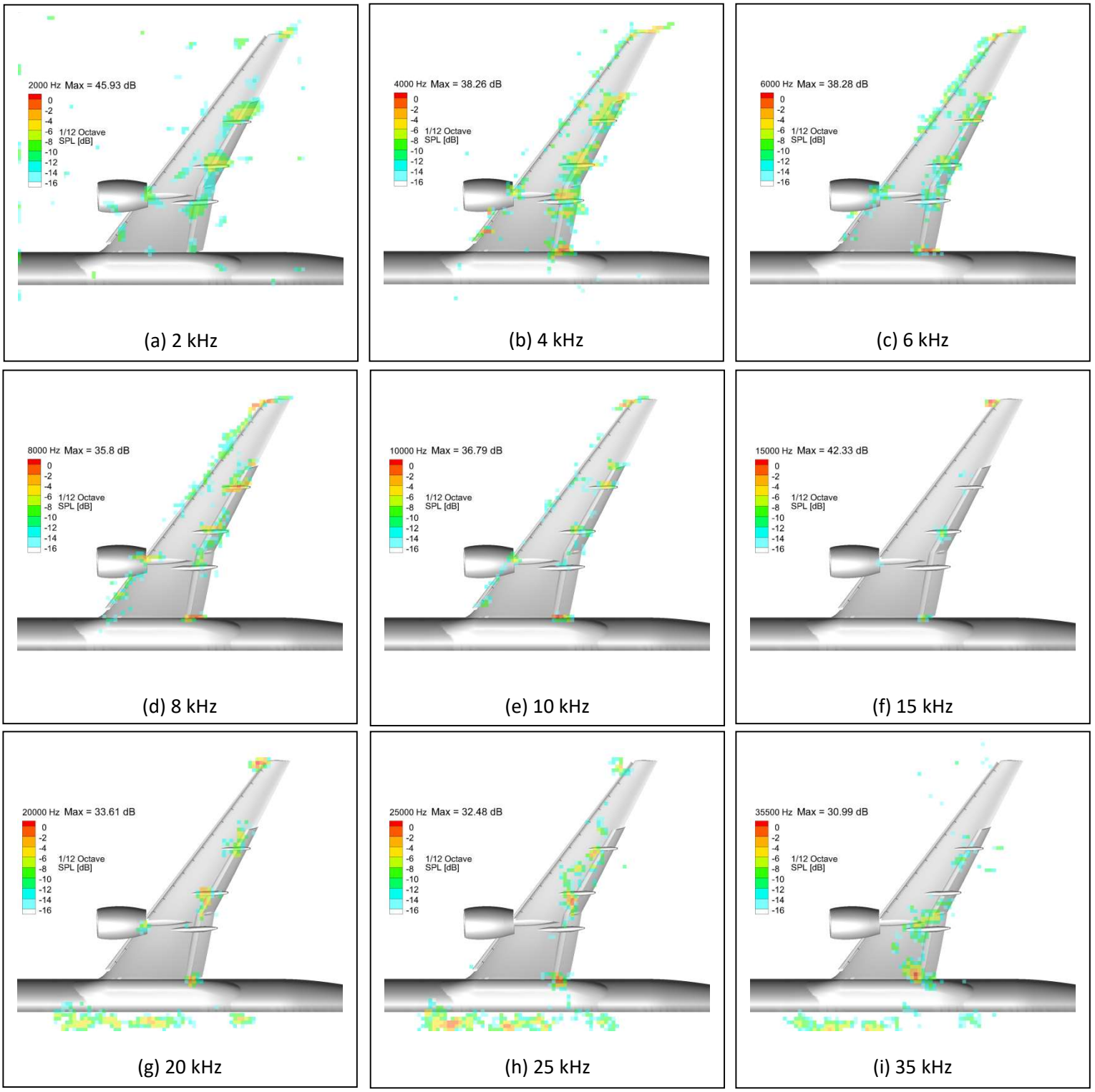

Fig. 37 1/12th-octave band MCF-DAMAS output.
PSS with SGF (Configuration 4), $\alpha = 8.5^{o}$, M = 0.16, $\phi = 90^{o}$.

bracket at 20 kHz.

A comparison of baseline PSS noise with noise generated when the SGF is added can be seen in Fig. 38. Similar to the FSS/SGF combination, the addition of the SGF to the PSS reduced the radiated noise by 10 dB for the majority of frequencies above 3 kHz. The Mach number scaling shown in Fig. 39 confirmed that this model configuration exhibited a sixth-power velocity scaling. There was an excellent collapse of the spectral levels below 5 kHz with a somewhat less successful collapse at higher frequencies. The directivity data shown in Fig. 40 confirmed that this model configuration displayed an approximate omnidirectional pattern over the ensemble of observer angles. The variation in spectral levels below 10 kHz was virtually identical to that shown in Fig. 36, although there was more variability in levels seen above 10 kHz for this configuration. In general, it can be concluded that the switch from Configuration 3 (FSS/SGF) to Configuration 4 (PSS/SGF) did not affect the radiated noise characteristics significantly, and that the

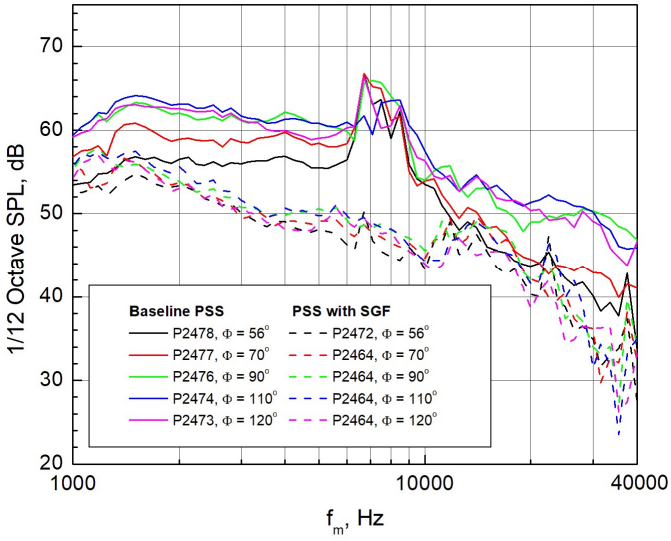

Fig. 38 Comparison of Configurations 2 and 4 (Baseline PSS and PSS with SGF), α = 8.5°, M = 0.16. Nacelle Installed for All Cases.

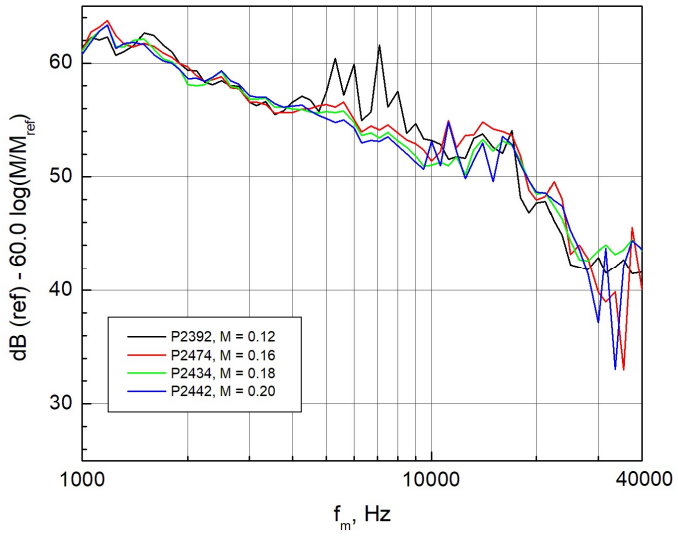

Fig. 39 PSS with SGF (Configuration 4) Mach Number Scaling, α = 8.5°, ϕ = 90°.

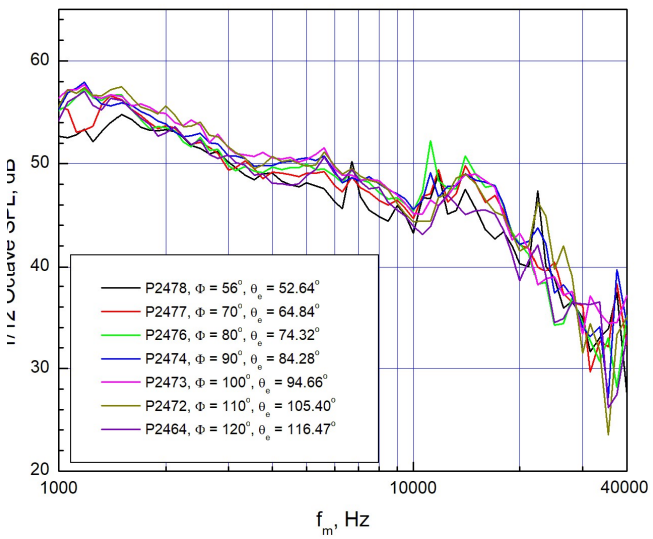

Fig. 40 PSS with SGF (Configuration 4) Directivity, α = 8.5°, M = 0.16.

addition of the flow-through nacelle had minimal impact on the observed noise.

5. Landing Gear Effects (Configurations 5 and 6)

A high-fidelity main landing gear (MLG) was developed for the CRM-HL model (Fig. 41a). The gear assembly included a four-wheel truck attached to a clevis (Fig. 41b) that allowed the truck angle to be set to -13˚, 0˚, or +13˚. High-fidelity components were constructed of stainless steel (load bearing) and nylon (nonload bearing) and included a door and scaled hydraulic lines and actuators. A partial landing gear bay was constructed within the main-element wing. Additional drawings and details of the landing gear assembly can be found in Ref. 26. For the MLG acoustic measurements shown here, the truck angle was set at a constant toe up angle of +13˚.

Figure 42 depicts MCF-DAMAS output for the FSS/SGF (Configuration 5) with the MLG attached. For this configuration, the noise was integrated over the wing region on the model. Not surprisingly, the MLG radiated noise was dominant. At lower frequencies (e.g., 2 kHz in the figure), flap bracket noise could also still be seen. With the SGF installed virtually, no slat noise was observed, with the one exception of residual outboard slat noise appearing at the wingtip at 2 kHz. It is noted that the MLG noise was not centered on the gear truck but was offset

(a)

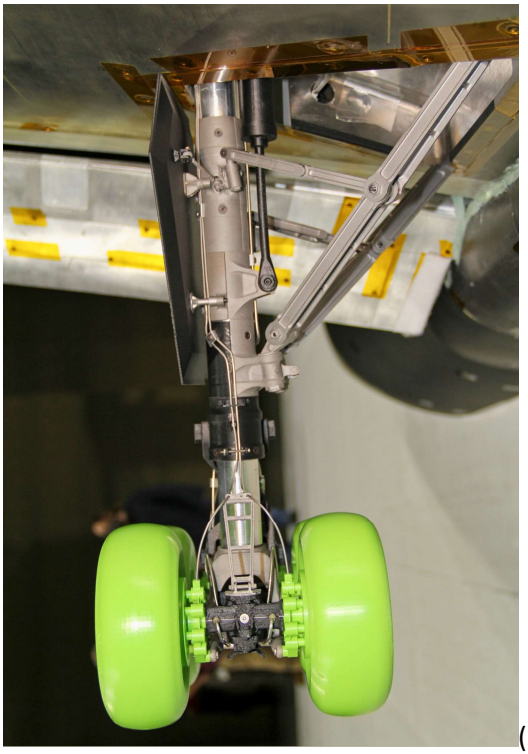

(b)

Fig. 41 High-fidelity Main Landing Gear:
(a) Position on Model, (b) Closeup View
[Source: NASA].

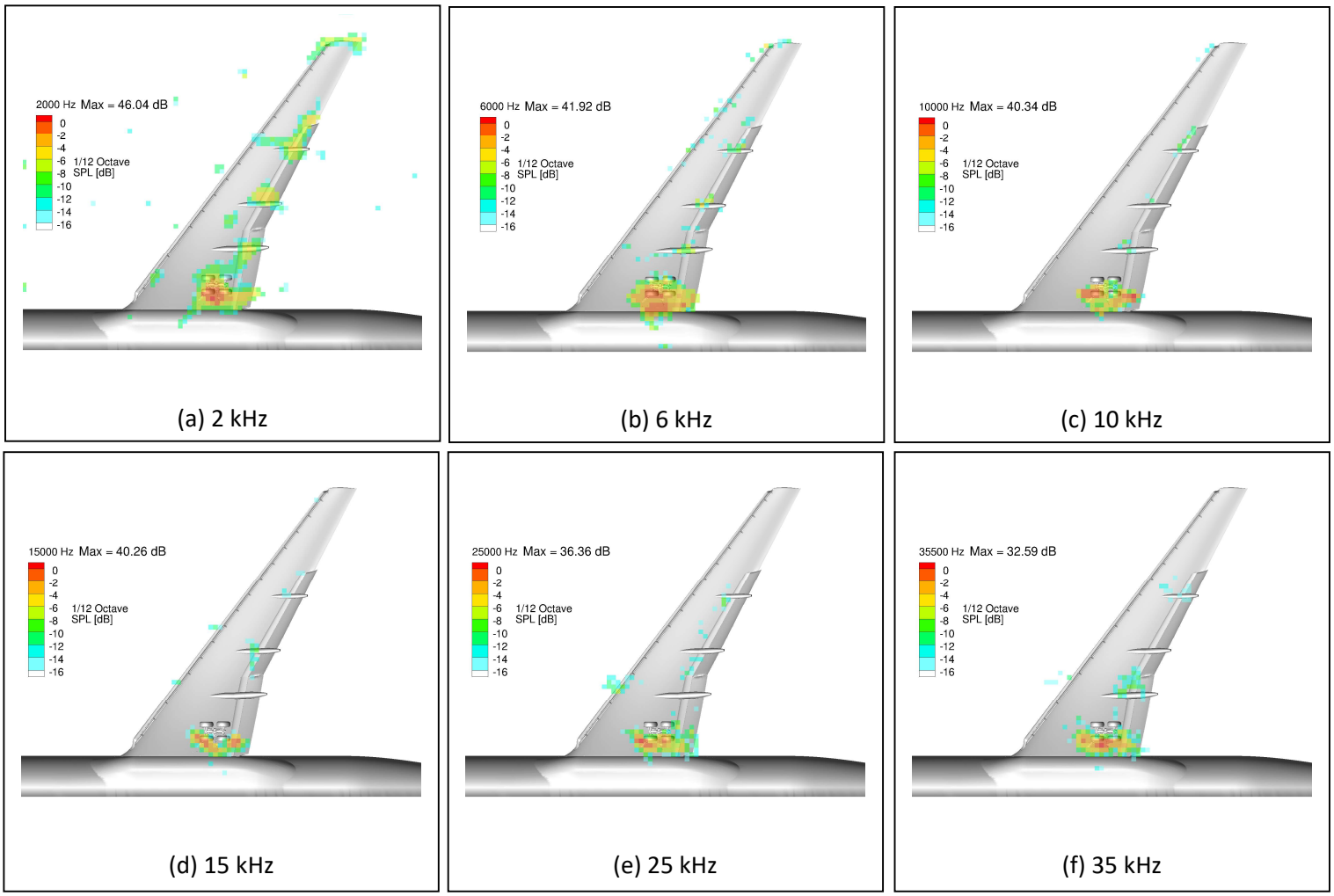

Fig. 42 1/12th-octave band MCF-DAMAS output.
FSS with SGF and MLG (Configuration 7), α = 8.5°, M = 0.16, ϕ = 90°.

to the inboard side where the retraction brackets reside. This could indicate increased noise radiation from the brackets, though uncertainties in the analysis made this difficult to state conclusively.

Figure 43 clearly shows the increase in noise for Configuration 5. For the baseline FSS configuration (the black line in Fig. 43), the addition of the gear (the green line) added approximately 2 – 3 dB to the spectral levels across the entire frequency range. The effect was more dramatic for the FSS/SGF configuration (the red line) where the deployment of the gear (the blue line) added 5 – 6 dB to the levels. Fortunately, in comparing the spectral levels for the FSS/MLG configuration with and without the SGF (green and blue lines), it was seen that the addition of the SGF lowered the observed noise levels by about 3 – 4 dB across the entire frequency range. Thus, the SGF provided an acoustic reduction benefit regardless of gear deployment for these configurations.

Figure 44 shows the Mach number scaling for the FSS/SGF/MLG combination. Previous investigations of scaled landing gear noise indicated a sixth-power velocity scaling behavior [56]. This is confirmed in Fig. 44 where an excellent collapse of the data was seen. Both the slat and landing gear contributed to a similar velocity scaling. There were strong tonal peaks shown at 7 kHz and 18 kHz, perhaps due to radiation from the flap brackets. These were seen in MCF-DAMAS outputs at Mach 0.12 for this configuration (not presented here).

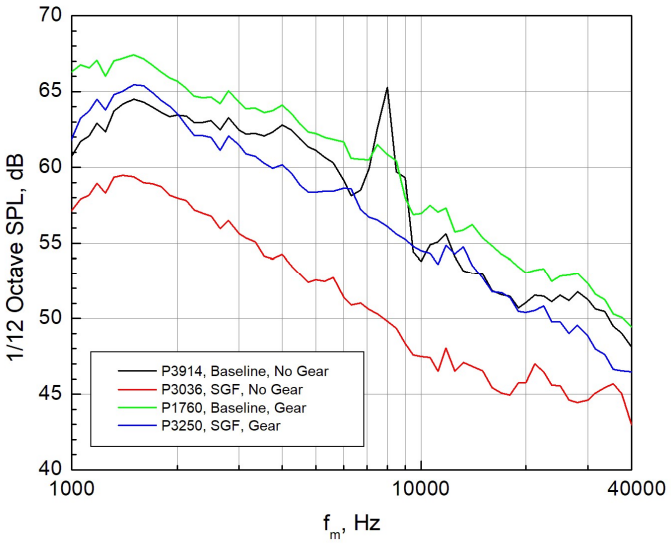

Fig. 43 FSS / MLG Noise Comparison. (Configuration 5), α = 8.5°, M = 0.16, ϕ = 90°. Integration over the wing region.

Similar MCF-DAMAS presentations to those shown in Fig. 42 can be seen in Fig. 45 for the PSS/SGF with the MLG deployed (Configuration 6). The noise radiation characteristics for the MLG were virtually identical as compared with Configuration 5, and the MLG dominated the noise observed for all frequencies in Fig. 45. This is not surprising since little to no slat / landing gear interaction was expected. Note that there were also no flap angle changes made that could influence the MLG noise. Figure 46 shows the increase in noise for the PSS/SGF/MLG configuration over the no-gear baseline. For the baseline FSS configuration (the black line in Fig. 43), the addition of the gear (the green line) added approximately 2 dB to the spectral levels across the entire frequency range. Using the PSS/SGF configuration (the red line) as a baseline, the deployment of the gear (the blue line) added 5 – 6 dB to the levels. The noise behavior observed between Configurations 5 and 6 was virtually identical. Finally, the Mach number scaling depicted in Fig. 47 again showed an excellent collapse of the spectra

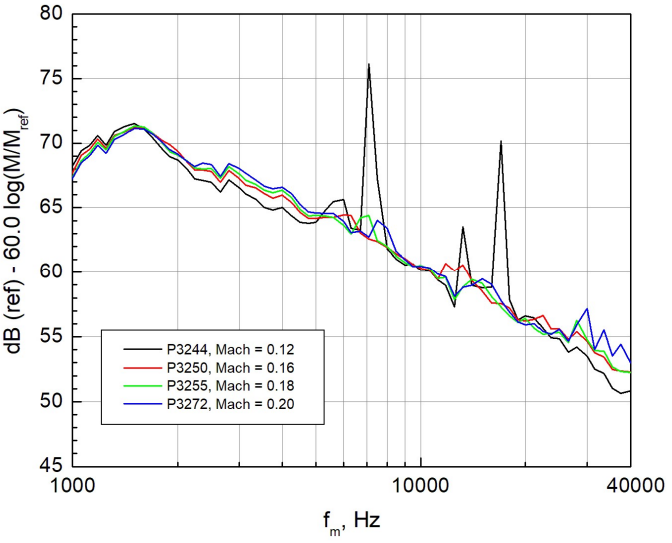

Fig. 44 FSS / MLG Mach Number Scaling. (Configuration 5), α = 8.5°, ϕ = 90°. Integration over the wing region.

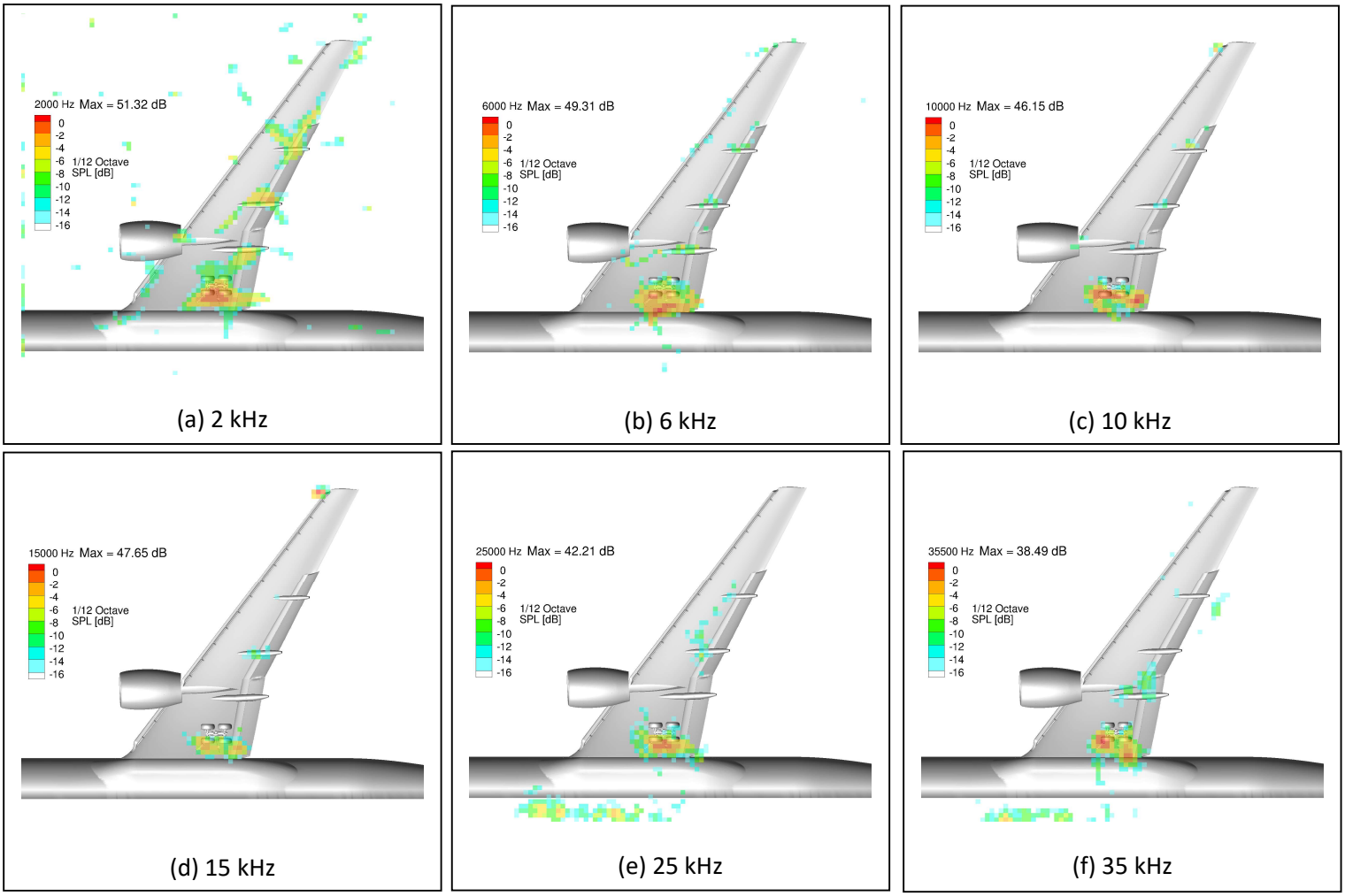

Fig. 45 MCF-corrected 1/12th-octave DAMAS output.
PSS with SGF and MLG (Configuration 6), α = 8.5°, M = 0.16, ϕ = 90°.

using a sixth-power scaling function. The same slat tones were observed as in Figure 44.

V. Summary

A detailed experimental study of the noise generated by a 10%-scale, semispan version of a High-Lift Common Research Model incorporating a leading-edge slat, trailing-edge flap and removable high-fidelity main landing gear was conducted in the open-jet test section of the NASA Langley 14- by 22-Foot Subsonic Tunnel. Aerodynamic and acoustic measurements were obtained on baseline and acoustically treated model configurations using surface pressure sensors and a traversing 97-microphone phased array that viewed the pressure side of the airframe. A modified version of the DAMAS array deconvolution method was employed to determine the locations and

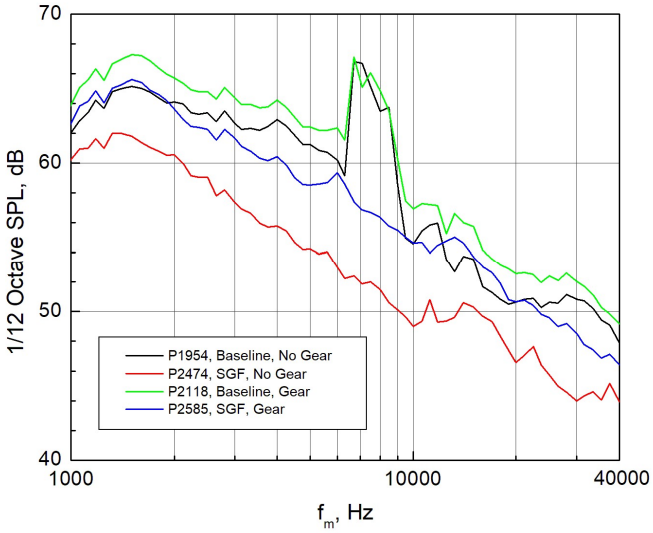

Fig. 46 PSS / MLG Noise Comparison. (Configuration 6), α = 8.5°, M = 0.16, ϕ = 90°. Integration over the wing region.

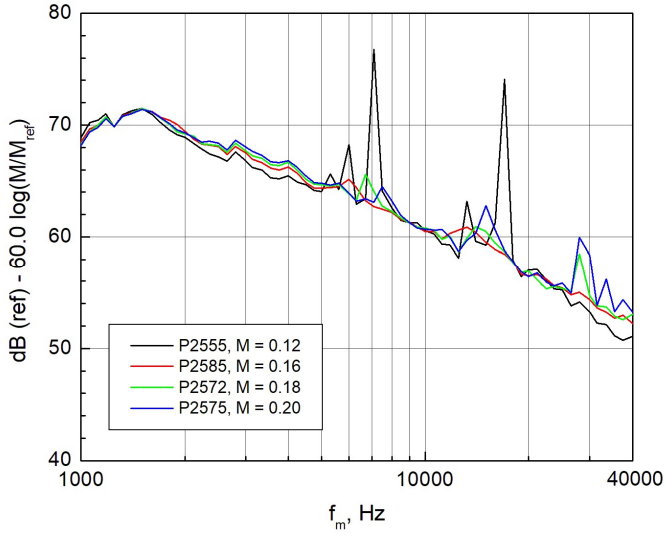

Fig. 47 PSS / MLG Mach Number Scaling. (Configuration 6), α = 8.5°, ϕ = 90°. Integration over the wing region.

strengths of relevant noise sources in the vicinity of the slat, flaps, and landing gear. Some primary conclusions derived from the study are as follows:

- Aerodynamic performance of the model at angles of attack around landing was preserved with the addition of the SGF to the FSS and PSS configurations. This was verified by examination of the model lift characteristics and the C_p distributions around the model. The experimental C_p distributions agreed well with computational results obtained from Powerflow simulations.
- The inclusion of the slat-gap filler with slat-tip transitions significantly reduced the radiated noise along the entire span of the slat, with typically 10 dB of noise reduction observed for the FSS/SGF and PSS/SGF configurations versus the baseline. There was some residual noise observed, especially near the wingtip, but not at significant levels. It can thus be concluded that the SGF is a very effective noise reduction mechanism for the slat.
- The flap noise was not a significant contributor to the overall radiated sound field for the baseline model configuration due to the stronger slat noise. With the addition of the SGF, the flap noise became more prominent but was still not a strong contributor to the overall noise. For certain configurations (Configuration 4 for instance), flap bracket noise could be observed for a number of frequencies due to the

reduction in slat noise. It is noted that the flap noise might be exacerbated in a real geometry due to interaction between the flap and the propulsive jet. This was not accounted for in the present study.

- Directivity measurements using the array at various observer locations revealed an approximate dipole directivity for the baseline FSS and PSS configurations. The incorporation of the SGF transitioned the radiated noise into an approximate omnidirectional pattern, although some residual variation with observer angle was seen, particularly for the PSS configurations.
- The observed Mach number variation implied a sixth-power dependency on flow speed, although this only applied to higher frequencies for the baseline FSS and PSS configurations, with a fifth-power dependency observed at lower frequencies. The addition of the SGF resulted in a true sixth-power dependency across the entire frequency range. This was a somewhat unexpected finding, and it's not entirely clear why the scaling changes with the addition of the SGF.
- As expected, the addition of the untreated main landing gear dramatically increased the overall spectral levels, with noise radiation appearing near the inboard side of the gear truck where the retraction brackets reside. This could indicate increased noise radiation from the brackets although this cannot be proved conclusively from the present data. There appeared to be no interaction between the slat and the landing gear in terms of overall noise levels. The SGF provided effective noise reduction regardless of gear deployment.

Although beyond the scope of the analyses described in this paper, future work could include an examination of slat-cove filler effects for comparison with the slat-gap filler. There were many additional model configurations tested beyond the ones described here that could provide a rich source of comparison data.

Acknowledgments

This work was sponsored by the NASA Advanced Air Transport Technology (AATT) Project in the Aeronautics Research Mission Directorate. The authors gratefully acknowledge the support and dedication of the 14- by 22-Foot Subsonic Tunnel staff, personnel from the NASA Langley Aeroacoustics, Structural Acoustics, and Computational Aerosciences Branches, and the many others who supported the test campaign.

References

[1] Hayes, J. A., Horne, W. C., Soderman, P. T., and Bent, P. H., "Airframe Noise Characteristics of a 4.7% Scale DC-10 Model," AIAA Paper 1997-1594, 3rd AIAA/CEAS Aeroacoustics Conference, Atlanta, GA, May 1997. https://doi.org/10.2514/6.1997-1594

[2] Storms, B. L., Ross, J. C., Horne, W. C., Hayes, J. A., Dougherty, R. P., Underbrink, J. R., Scharpf, D. F., and Moriarty, P. J., "An Aeroacoustic Study of an Unswept Wing with a Three-Dimensional High Lift System," NASA Technical Memorandum 112222, February 1998.

[3] Dobrzynski, W., Nagakura, K., Gehlhar, B., and Buschbaum, A., "Airframe Noise Studies on Wings with Deployed High-Lift Devices," AIAA Paper 1998-2337, 4th AIAA/CEAS Aeroacoustics Conference, Toulouse, France, June 1998. https://doi.org/10.2514/6.1998-2337

[4] Storms, B. L., Hayes, J. A., Moriarty, P. J., and Ross, J. C., "Aeroacoustic Measurements of Slat Noise on a Three-Dimensional High-Lift System," AIAA Paper 1999-1957, 5th AIAA/CEAS Aeroacoustics Conference, Bellevue, WA, May 1999. https://doi.org/10.2514/6.1999-1957

[5] Choudhari, M. M., Lockard, D. P., Macaraeg, M. G., Singer, B. A., Streett, C. L., Neubert, G. R., Stoker, R. W., Underbrink, J. R., Berkman, M. E., Khorrami, M. R., and Sadowski, S. S., "Aeroacoustic Experiments in the Langley Low-Turbulence Pressure Tunnel," NASA Technical Memorandum 211432, February 2002.

[6] Mendoza, F., and Brooks, T., "Aeroacoustic Measurements of a Wing/Slat Model," AIAA Paper 2002-2604, 8th AIAA/CEAS Aeroacoustics Conference, Breckenridge, CO, June 2002. https://doi.org/10.2514/6.2002-2604

[7] Terracol, M., Manoha, E., and Lemoin, B., "Noise Sources Generation in a Slat Cove: Hybrid Zonal RANS/LES Simulation and Dedicated Experiment," AIAA Paper 2011-3203, 20th AIAA Computational Fluid Dynamics Conference, Honolulu, HI, June 2011. https://doi.org/10.2514/6.2011-3203

[8] Chow, L. C., Mau, K., and Remy, H., "Landing Gears and High Lift Devices Airframe Noise Research," AIAA Paper 2002-2408, 8th AIAA/CEAS Aeroacoustics Conference, June 2002. https://doi.org/10.2514/6.2002-2408

[9] Guo, Y.P., "A Model for Slat Noise Generation", AIAA Paper 1997-1647, 3rd AIAA/CEAS Aeroacoustics Conference, Atlanta, GA, May 1997. https://doi.org/10.2514/6.1997-1647

[10] Singer, B.A., Lockard, D.P., Brentner, K.S., Khorrami, M.R., Berkman, M.E., and Choudhari, M., "Computational Aeroacoustic Analysis of Slat Trailing-Edge Flow", AIAA Paper 1999-1802, 5th AIAA/CEAS Aeroacoustics Conference, Bellevue, WA, May 1999. https://doi.org/10.2514/6.1999-1802

[11] Guo, Y.P., "A Discrete Vortex Model for Slat Noise Prediction", AIAA Paper 2001-2157, 7th AIAA/CEAS Aeroacoustics Conference, Maastricht, Netherlands, May 2001. https://doi.org/10.2514/6.2001-2157

[12] Dobrzynski, W., and Pott-Pollenske, M., "Slat Noise Source Studies for Farfield Noise Prediction", AIAA Paper 2001-2158, 7th AIAA/CEAS Aeroacoustics Conference, Maastricht, Netherlands, May 2001. https://doi.org/10.2514/6.2001-2158

[13] Mendoza, J.M., Brooks, T.F., and Humphreys, W.M., Jr., "An Aeroacoustic Study of a Leading Edge Slat Configuration", *International Journal of Aeroacoustics*, Vol. 1, No. 3, 2002, pp. 241-274. https://doi.org/10.1260/147547202320962583

[14] Moriarty, P.J., and Heineck, J.T., "PIV Measurements Near a Leading Edge Slat", Proceedings of the 3rd International Workshop on Particle Image Velocimetry (PIV), September 1999.

[15] Choudhari, M., and Lockard, D.P., "Assessment of Slat Noise Predictions for 30P30N High-Lift Configuration from BANC-III Workshop", AIAA Paper 2015-2844, 21st AIAA/CEAS Aeroacoustics Conference, Dallas, TX, June 2015. https://doi.org/10.2514/6.2015-2844

[16] Zhang, Y, Richardson, R., Cattafesta, L.N., Pascioni, K.A., Choudhari, M.M., Lockard, D.P., Khorrami, M.R., and Turner, T.L., "Slat Noise Control Using a Slat Gap Filler", AIAA Paper 2020-2553, AIAA Aviation Forum (Virtual), June 2020. https://doi.org/10.2514/6.2020-2553

[17] Yamamoto, K., Murayama, M., Isotani, K., Ueno, Y., Hayashi, K., and Hirai, T., "Slat Noise Reduction Based on Turbulence Attenuation Downstream of Shear-layer Reattachment", AIAA Paper 2022-2954, 28th AIAA/CEAS Aeroacoustics Conference, Southampton, UK, June 2022. https://doi.org/10.2514/6.2022-2954

[18] Bahr, C.J., "Accounting for the Influence of Decorrelation in Microphone Phased Array Deconvolution Methods", AIAA Paper 2022-2814, 28th AIAA/CEAS Aeroacoustics Conference, Southampton, UK, June 2022. https://doi.org/10.2514/6.2022-2814

[19] Lin, J. C., Melton, L. G., Hannon, J. A., Andino, M. Y., Koklu, M., Paschal, K. B., and Vatsa, V. N., "Wind Tunnel Testing of Active Flow Control on the High Lift Common Research Model", AIAA Paper 2019-3723, AIAA Aviation 2019 Forum, Dallas, TX, 2019. https://doi.org/10.2514/6.2019-3723

[20] Khorrami, M. R., Humphreys, W. M., Lockard, D. P., and Ravetta, P. A., "An Assessment of Flap and Main Landing Gear Noise Abatement Concepts", AIAA Paper 2015-2978, 21st AIAA/CEAS Aeroacoustics Conference, Dallas, TX, 2015. https://doi.org/10.2514/6.2015-2978

[21] Lockard, D. P., Choudhari, M. M., Vatsa, V. N., O'Connell, M. D., Duda, B. M., and Fares, E., "Noise Simulations of the High-Lift Common Research Model", AIAA Paper 2017-3362, 23rd AIAA/CEAS Aeroacoustics Conference, Denver, CO, 2017. https://doi.org/10.2514/6.2017-3362

[22] Lockard, D. P., O'Connell, M. D., Vatsa, V. N., and Choudhari, M. M., "Assessment of Aeroacoustic Simulations of the High-Lift Common Research Model", AIAA Paper 2019-2460, 25th AIAA/CEAS Aeroacoustics Conference, Delft, The Netherlands, 2019. https://doi.org/10.2514/6.2019-2460

[23] Turner, T.L., and Long, D.L., "Development of a SMA-Based, Slat-Gap Filler for Airframe Noise Reduction", AIAA Paper 2015-0730, AIAA SciTech 2015 Forum, Kissimmee, FL, January 2015. https://doi.org/10.2514/6.2015-0730

[24] Turner, T.L., Mulvaney, J.W., Lockard, D.P,, Allen, R.A., and Brynildsen, S.E., "Development of Slat Gap and Slat Cove Filler Treatments for Noise Reduction Assessment on the High-Lift Common Research Model in the NASA LaRC 14x22", AIAA Paper 2022-2989, 28th AIAA/CEAS Aeroacoustics Conference, Southampton, UK, June 2022. https://doi.org/10.2514/6.2022-2989

[25] Hutcheson, F.V., Lockard, D.P., and Stead, D.J., "On the Alleviation of Background Noise for the High-Lift Common Research Model Aeroacoustic Test", AIAA Paper 2022-2988, 28th AIAA/CEAS Aeroacoustics Conference, Southampton, UK, June 2022. https://doi.org/10.2514/6.2022-2988

[26] Lacy, D.S., and Sclafani, A.J., "Development of the High Lift Common Research Model (HL-CRM): A Representative High Lift Configuration for Transonic Transports", AIAA Paper 2016-0308, AIAA SciTech 2016 Forum, San Diego, CA, January 2016. https://doi.org/10.2514/6.2016-0308

[27] Fell, J.S., Webb, S.R., Laws, C.T., Snyder, M.L., and Rhew, R.D., "Development of the 10% NASA High-Lift Common Research Model (CRM-HL)", AIAA Paper 2021-0385, AIAA SciTech 2021 Forum (Virtual), January 2021. https://doi.org/10.2514/6.2021-0385

[28] Lockard, D.P., Turner, T.L., Bahr, C.J., and Hutcheson, F.V., "Overview of Aeroacoustic Testing of the High-Lift Common Research Model", AIAA Paper 2021-2113, AIAA Aviation 2021 Forum (Virtual), August 2021. https://doi.org/10.2514/6.2021-2113

[29] High Lift Prediction Workshop 3 - Geometry Files (nasa.gov)

[30] Streett, C.L., Casper, J.H., Lockard, D.P., Khorrami, M.R., Stoker, R.W., Elkoby, R., Wenneman, W.F., and Underbrink, J.R., "Aerodynamic Noise Reduction for High-Lift Devices on a Swept Wing Model", AIAA Paper 2006-0212, 44th Aerospace Sciences Meeting, Reno, NV, January 2006. https://doi.org/10.2514/6.2006-212

[31] Scholten, W.D., Hartl, D.J., Turner, T.L., and Kidd, R.T., "Development and Analysis-Driven Optimization of Superelastic Slat-Cove Fillers for Airframe Noise Reduction", *AIAA Journal*, Volume 54, No. 3, 2016, pp. 1074-1090, 2016. https://doi.org/10.2514/1.J054011

[32] Humphreys, W. M., Brooks, T. F., Bahr, C. J., Spalt, T. B., Bartram, S. M., Culliton, W. G., and Becker, L. E., "Development of a Microphone Phased Array Capability for the Langley 14- by 22-Foot Subsonic Tunnel", *AIAA Paper 2014-2343*, 20th AIAA/CEAS Aeroacoustics Conference, Atlanta, GA, June 2014. https://doi.org/10.2514/6.2014-2343

[33] Humphreys, W. M., Jr., "Microphone Phased Array NetCDF/HDF5 Archival Files: Application Program Interface Reference", *NASA Technical Memorandum 2019-220402*, September 2019. https://ntrs.nasa.gov/citations/20190031820

[34] Bahr, C. J. and Horne, W. C., "Subspace-based Background Subtraction Applied to Aeroacoustic Wind Tunnel Testing", *International Journal of Aeroacoustics*, Vol. 16, Nos. 4 & 5, 2017, pp. 299-325. https://doi.org/10.1177/1475472X17718885

[35] Hald, J., "Removal of Incoherent Noise from an Averaged Cross Spectral Matrix", *Journal of the Acoustical Society of America*, Vol. 142, No. 2, 2017, pp. 846-854. https://doi.org/10.1121/1.4997923

[36] Brooks, T. F., and Humphreys, W. M., "A Deconvolution Approach for the Mapping of Acoustic Sources (DAMAS) Determined from Phased Microphone Arrays", *Journal of Sound and Vibration*, Vol. 294, Nos. 4 & 5, 2006, pp. 856-879. https://doi.org/10.1016/j.jsv.2005.12.046

[37] Bahr, C.J., and Lockard, D.P., "Designing Shading Schemes for Microphone Phased Arrays", BeBeC-2020-S1, 2020 Berlin Beamforming Conference, Berlin, Germany, March 2020. https://www.bebec.eu/fileadmin/bebec/downloads/bebec-2020/papers/BeBeC-2020-S01.pdf

[38] Chen, H., "Volumetric Formulation of the Lattice Boltzmann Method for Fluid Dynamics: Basic Concept", *Physical Review E*, Vol. 58, September 1998, pp. 3955–3963. https://doi.org/10.1103/PhysRevE.58.3955

[39] Chen, H., Teixeira, C., and Molvig, K., "Realization of Fluid Boundary Conditions via Discrete Boltzmann Dynamics", *International Journal of Modern Physics C*, Vol. 9, No. 8, 1998, pp. 1281–1292. https://doi.org/10.1142/S0129183198001151

[40] Yakhot, V. and Orszag, S., "Renormalization Group Analysis of Turbulence. I. Basic Theory", *Journal of Scientific Computing*, Vol. 1, No. 2, 1986, pp. 3–51. https://doi.org/10.1007/BF01061452

[41] Chen, H., Kandasamy, S., Orszag, S., Shock, R., Succi, S., and Yakhot, V., "Extended Boltzmann Kinetic Equation for Turbulent Flows", Science, Vol. 301, No. 5633, 2003, pp. 633–636. https://doi.org/10.1126/science.1085048

[42] Chen, H., Orszag, S., Staroselsky, I., and Succi, S., "Expanded Analogy between Boltzmann Kinetic Theory of Fluid and Turbulence", *Journal of Fluid Mechanics*, Vol. 519, November 2004, pp. 301–314. https://doi.org/10.1017/S0022112004001211

[43] Chen, S. and Doolen, G., "Lattice Boltzmann Method for Fluid Flows", *Annual Review of Fluid Mechanics*, Vol. 30, January 1998, pp. 329–364. https://doi.org/10.1146/annurev.fluid.30.1.329

[44] Shan, X., Yuvan, X-F., and Chen, H., "Kinetic Theory Representation of Hydrodynamics: a Way Beyond the Navier-Stokes Equation", *Journal of Fluid Mechanics*, Vol. 550, 2006, pp. 413-441. https://doi.org/10.1017/S0022112005008153

[45] Zhuo, C., Zhong, C., Li, K., Xiong, S., Chen, X., and Cao, J., "Application of Lattice Boltzmann Method to Simulation of Compressible Turbulent Flow", *Communications Computer Physics*, Vol. 8, 2010, pp. 1208–1223. https://doi.org/10.4208/cicp.300110.070510a

[46] Koenig, B. and Fares, E., "Validation of a Transonic Lattice-Boltzmann Method for the NASA Common Research Model", AIAA Paper 2016-2023, 54th AIAA Aerospace Sciences Meeting, San Diego, CA, January 2016. https://doi.org/10.2514/6.2016-2023

[47] Fares, E. and Nölting, S., "Unsteady Flow Simulation of a High-Lift Configuration using a Lattice Boltzmann Approach", AIAA Paper 2011-0869, 49th AIAA Aerospace Sciences Meeting, Orlando, FL, January 2011. https://doi.org/10.2514/6.2011-869

[48] Fares, E., Wessels, M., Li, Y., Gopalakrishnan, P., Zhang, R., Sun, C., Gopalaswamy, N., Roberts, P., Hoch, J., and Chen, H., "Validation of a Lattice Boltzmann Approach for Transonic and Supersonic Simulations", AIAA Paper 2014-0952, 52nd Aerospace Sciences Meeting, National Harbor, MD, January 2014. https://doi.org/10.2514/6.2014-0952

[49] Fares, E., Casalino, D., and Khorrami, M., "Evaluation of Airframe Noise Reduction Concepts via Simulations Using a Lattice Boltzmann Approach", AIAA Paper 2015-2988, 21st AIAA/CEAS Aeroacoustics Conference, Dallas, TX, 2015. https://doi.org/10.2514/6.2015-2988

[50] Khorrami, M., Fares, E., and Casalino, D., "Towards Full-Aircraft Airframe Noise Prediction: Lattice-Boltzmann Simulations", AIAA Paper 2014-2481, 20th AIAA/CEAS Aeroacoustics Conference, Atlanta, GA, June 2014. https://doi.org/10.2514/6.2014-2481

[51] Lockard, D. P., Choudhari, M. M., and Vatsa, V. N., "Aeroacoustic Simulations of the High-Lift Common Research Model and Validation with Experiment", AIAA Paper 2022-2806, 28th AIAA/CEAS Aeroacoustics Conference, Southampton, UK, June 2022. https://doi.org/10.2514/6.2022-2806

[52] Pascioni, K. A. and Cattafesta, L. N., "Unsteady Characteristics of a Slat-Cove Flow Field", *Physical Review Fluids*, Vol. 3, No. 3, 034607, 2018. https://doi.org/10.1103/PhysRevFluids.3.034607

[53] Amiet, R. K., "Refraction of Sound by a Shear Layer", *Journal of Sound and Vibration*, Vol. 58, No. 4, 1978, pp. 467-482. https://doi.org/10.1016/0022-460X(78)90353-X

[54] Jawahar, H.K., Meloni, S., Camussi, R., and Azarpeyvand, M., "Intermittent and Stochastic Characteristics of Slat Tones", *Physics of Fluids*, Vol. 33, 025120, 2021. https://doi.org/10.1063/5.0033827

[55] Ahlefeldt, T., "Microphone Array Measurement in European Transonic Wind Tunnel at Flight Reynolds Numbers", *AIAA Journal*, Vol. 55, No. 1, 2017, pp. 36-48. https://doi.org/10.2514/1.J055262

[56] Humphreys, W.M., Jr., and Brooks, T.F., "Noise Spectra and Directivity for a Scale-Model Landing Gear", *International Journal of Aeroacoustics*, Vol. 8, No. 5, 2009, pp. 409-443. https://doi.org/10.1260/147547209788549316